

A generalized multi-component analytical method to study the performance of a rockfall barrier under a generic impact condition

Original

A generalized multi-component analytical method to study the performance of a rockfall barrier under a generic impact condition / Pimpinella, Francesco; Marchelli, Maddalena; De Biagi, Valerio. - In: COMPUTERS AND GEOTECHNICS. - ISSN 0266-352X. - 188:(2025), pp. 1-19. [10.1016/j.compgeo.2025.107602]

Availability:

This version is available at: 11583/3002752 since: 2025-09-03T10:17:21Z

Publisher:

Elsevier

Published

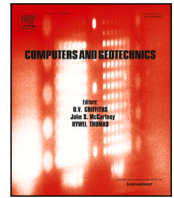
DOI:10.1016/j.compgeo.2025.107602

Terms of use:

This article is made available under terms and conditions as specified in the corresponding bibliographic description in the repository

Publisher copyright

(Article begins on next page)



Research paper

A generalized multi-component analytical method to study the performance of a rockfall barrier under a generic impact condition

Francesco Pimpinella ^a ,* Maddalena Marchelli ^b , Valerio De Biagi ^a 

^a Department of Structural, Geotechnical and Building Engineering, Politecnico di Torino, Duca degli Abruzzi, 24, Torino, 10129, TO, Italy

^b Department of Environment, Land and Infrastructure Engineering, Politecnico di Torino, Duca degli Abruzzi, 24, Torino, 10129, TO, Italy

ARTICLE INFO

Keywords:

Flexible rockfall barriers
Global analytical approach
Impact position
Structural efficiency

ABSTRACT

The design of rockfall barriers is based on the system's ability to absorb and dissipate the energy of an impacting block. Although manufacturers have developed different solutions, leading to countless possible on-site installations, the functional components of rockfall barriers remain largely consistent across technologies. In this study, the mechanical behaviour of a generic system is evaluated proposing a global analytical method, derived from the appropriate assembly of its fundamental components. For a given impact energy and position, this model allows estimating the barrier response in terms of maximum deflection of the net, forces in the wire ropes and energy dissipated by dissipating devices, providing an easy-to-use tool for the design. The method is applied to a 1000 kJ rockfall barrier. As real-scale test results are available for centred impacts only, a numerical model was developed to extend the validation to eccentric load cases. Besides being used for design purposes, the model can be utilized in a maintenance plan to assess the most critical components under various impact scenarios.

1. Introduction

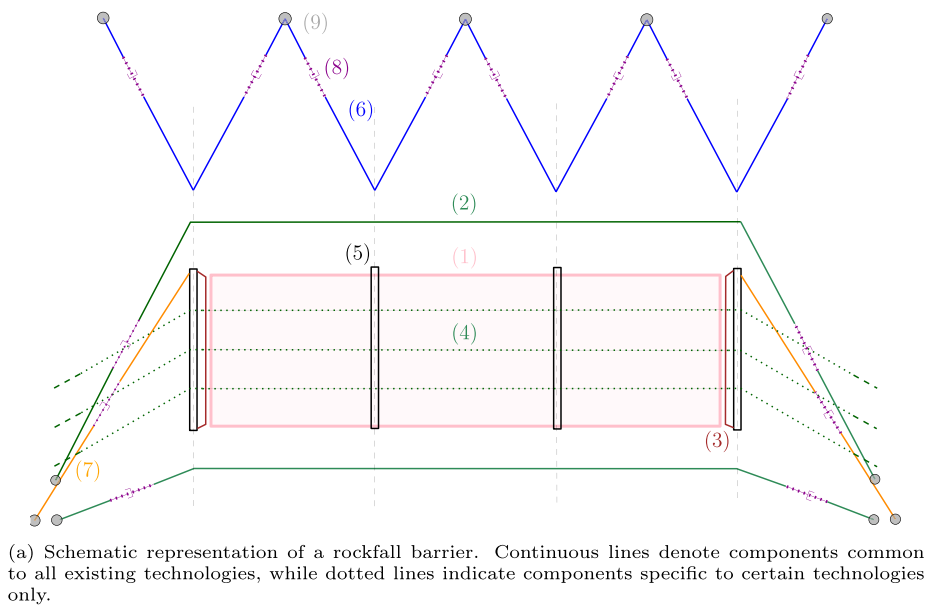
Flexible rockfall barriers are widely used across the globe as a passive mitigation measure in alpine and coastal environments to protect structures and infrastructure. These barriers offer the advantages of easy installation, along with relatively low environmental and economic costs (Volkwein et al., 2011; Yang et al., 2019). In the event of a rockfall, they can withstand high impact energies (up to 12,500 kJ) despite being lightweight structures. Their design ensures effective energy dissipation by distributing loads in multiple directions and concentrating damage on sacrificial components. These components are specifically designed to be replaceable after a rockfall event, allowing the barrier to remain functional (Yang et al., 2019).

Although different manufacturers have adopted various design philosophies over time, the basic assembly of a generic system is common to the majority of existing technologies. Generally speaking, the initial load distribution function is consistently assigned to an intercepting structure ((1) in Fig. 1(a)), which spans the entire barrier and serves as a protective shield positioned along the slope. The intercepting structure consists of a net made of metallic cables or wires, which bears the direct strike of the impactor, deforms elastically and/or plastically, and transmits the stresses to the other components (Peila and Ronco, 2009). As the first component hit by falling impactors, the intercepting structure must exhibit both high resistance and flexibility

to effectively stop the impactors while distributing the loads evenly to prevent localized concentrations (Maheshwari et al., 2023). Usually, a mesh finer than the principal net is present to retain impactors smaller than the spacing in the principal net. The loads are then primarily transferred to longitudinal and transversal (vertical) wire ropes ((2) and (3) in Fig. 1(a), respectively), also called panel wire ropes, as they are directly linked to the intercepting structure. These wire ropes can be positioned either solely along the edges of the net panels or integrated within the panels themselves as transmission ropes ((4) in Fig. 1(a)). This latter solution is mainly used in semi-rigid systems (Mentani, 2015), where a more uniform load distribution is achieved to maintain limited out-of-plane deformations (Van Tran et al., 2012, 2013; Zhao et al., 2022a). The whole system is kept in place by steel posts ((5) in Fig. 1(a)), which constitute the support system, and by upslope and lateral wire ropes ((6) and (7) in Fig. 1(a), respectively). These ropes are also referred to as sustaining ropes. Steel posts are generally connected to concrete foundations through hinged connections, while wire ropes are anchored to the ground using injected cables or grouted bars. Wire ropes are usually the location of dissipating devices, also called brakes ((8) in Fig. 1(a)), i.e., the elements responsible for dissipating up to 80% of the total incoming energy and providing additional flexibility to the structure (Zhang et al., 2023; Pimpinella et al., 2024a),

* Corresponding author.

E-mail address: francesco.pimpinella@polito.it (F. Pimpinella).



(b) Courtesy of Geobrugg AG

Fig. 1. Scheme of the generic rockfall barrier assembly (a) and installation example (b)

according to their number and properties. The number, configuration, location, and type of dissipating devices depend strictly on the specific technology and manufacturer. Clamps and wire rope clips serve as connecting components between the main elements. To ensure the proper system flexibility in load cases foreseeing impacts close to the steel post, the intercepting structure must not be constrained at the intermediate posts terminations. This possibly detrimental constraint is generally avoided adopting one of the following solutions in regions close to intermediate posts: (i) transitional ropes can be inserted as a connection with longitudinal ropes at both sides of the posts; (ii) fuse elements can be used to connect the intercepting structure and longitudinal ropes; or (iii) the assembly can be configured so that the intercepting structure exhibits a looser condition in that area.

In the current design framework (EN 1997-1:2004, 2004), as defined by European (EAD 340059-00-0106, 2018) and Swiss (Gerber, 2001) certification procedures, the performance of flexible rockfall barriers is characterized by two energy absorption levels: the Maximum Energy Level (MEL) and the Service Energy Level (SEL). These are assessed through standardized impact tests, which involve striking the centre of the central module in a three-module barrier system. A system is considered to have failed if it does not intercept or arrest the impactor, or if it fails to meet specific performance requirements as in Gerber (2001) and EAD 340059-00-0106 (2018).

However, since the adoption of these procedures, numerous numerical (Koo et al., 2016; Mentani et al., 2017; Toe et al., 2018; Zhao et al.,

2020) and experimental (Caviezel et al., 2022) studies have questioned the representativeness of such tests under real-world impact conditions. These investigations have demonstrated that standardized impacts do not adequately capture the full range of possible scenarios or the most critical loading conditions. For example, the size and shape of the impactor significantly influence the mechanical response of the barrier (Koo et al., 2016; Yu et al., 2021), while the impact location plays a crucial role in activating specific energy dissipation mechanisms (Qi et al., 2018a; Zhao et al., 2020; Caviezel et al., 2022). Regardless of intercepting structure typology, both isolated net panels (Cazzani et al., 2002; Pimpinella et al., 2025) and complete barrier systems (Cazzani et al., 2002; Zhao et al., 2020; Caviezel et al., 2022; Douthe et al., 2022) have shown high sensitivity to eccentric impacts, highlighting the limitations of describing barrier capacity using a single, centrally tested energy value. To partially address these limitations, the Swiss directive (Gerber, 2001) introduced amplification factors intended to better reflect the system's actual capacity, which depends on a complex interplay of variables. However, this adjustment remains insufficient, as it does not fully capture the variability and complexity of real-world impact scenarios.

Due to the high cost and complexity of full-scale testing, many researchers have relied on numerical simulations to investigate the global mechanical behaviour of flexible barriers under varied impact conditions (Gentilini et al., 2012, 2013; Escallón et al., 2014; Xu et al., 2018a; Coulibaly et al., 2019; Yu et al., 2021; Jin et al., 2021).

Nevertheless, the range of impact scenarios that can be explored remains limited due to the significant computational resources required. Although simplified numerical models of key components can reduce simulation time (Jin et al., 2021), model development remains time-consuming and highly specific to each technology. As a result, obtaining a comprehensive distribution of system capacity often proves impractical. Although these models are not readily applicable for investigating the full range of possible impact conditions, they have been, and continue to be, used to validate analytical theories at both the component (Castro-Fresno et al., 2009; Castanon-Jano et al., 2019; Pimpinella et al., 2025) and system scales (Yu et al., 2018).

Meta-models calibrated using a set of finite element simulations have emerged as a promising and high-potential alternative for evaluating system performance (Toe et al., 2018; Lambert et al., 2020). Even in this case, a numerical model specifically tailored to the technology is required, as it defines the application domain of the meta-model. However, key advantages of the approach include its ability to generate large datasets, with results that implicitly account for a wide range of realistic impact conditions and the ageing behaviour of components (Chen et al., 2021; Xu et al., 2024), and the possibility of formulating the meta-model to predict only selected performance indicators, rather than the complete system response. On the other hand, the inherently higher level of abstraction in meta-models can make it challenging to identify the barrier's critical components, especially when the barrier exhibits strong local variations in its response.

Analytical models may therefore offer a more general and efficient means of evaluating barrier performance. Early studies treated rockfall barriers as single-degree-of-freedom oscillators (Cantarelli and Giani, 2006) or pseudo-bidimensional structures (Peila et al., 1998). More recent formulations based on idealized load paths have enabled energy absorption estimates for chain-link meshes (Hambleton et al., 2012) and ring nets (Guo et al., 2020). System-level analytical models have also been developed to estimate maximum deflection (Yu et al., 2018) and post-impact residual energy dissipation capacity (Zhang et al., 2023). In both cases, total energy dissipation is primarily attributed to dissipating devices, with fixed correction factors accounting for other components such as net deformation and friction. These components are thus treated from a purely geometrical perspective. It is well established that centrally located impacts do not represent the most demanding force or deflection scenarios (Bourrier et al., 2015; Koo et al., 2016; Zhao et al., 2020; Eicher et al., 2023), and current models do not allow for the quantification of energy dissipation in non-dissipator components under eccentric impacts, where asymmetrical behaviour emerges. In Zhang et al. (2023), for instance, barrier performance is expressed solely as the ratio between energy dissipated by dissipating devices and the nominal energy level.

Some detailed analytical models for individual components have been proposed. Guo et al. (2020, 2022) have developed a model for ring-net panels that accurately predicts maximum deflection and energy dissipation. Hambleton et al. (2012) have proposed a general model for the load–displacement behaviour of chain-link nets, while Han et al. (2025) extended this to include reinforcing strands. Pimpinella et al. (2024a) have presented a model for evaluating the performance of widely used dissipating devices, and Lu and Yu (2003) have provided formulations for various dissipation mechanisms in structural and mechanical components. For steel wire ropes, advanced geometrically based models have been proposed (Wang et al., 2015; De Menezes and Marczak, 2021), and general guidelines for estimating their force–displacement behaviour and failure loads are available in Feyrer (2007).

To the best of the authors' knowledge, no existing analytical formulation enables the estimation of energy dissipation across all barrier components under non-centred impact conditions. Furthermore, no current model can be readily adapted to the full range of barrier technologies. This study therefore aims to propose a generalized analytical approach for evaluating the performance of flexible rockfall barriers

under arbitrary impact conditions, by quantifying the energy dissipation contributions of each component. The proposed methodology is designed to be adaptable to any barrier configuration.

The structure of the paper is as follows. Section 2 presents the general framework for constructing the multi-component analytical model for flexible rockfall barriers and outlines the simplifying assumptions underlying the model. The mechanical behaviour of each component is detailed in Section 3, followed by model assembly and calibration in Section 4. A case study involving the RXI-100 system by Geobrugg AG is presented in Section 5, where the analytical model is tailored to this specific technology (Section 5.1) and supported by a numerical model (Section 5.2) to extend validation to eccentric impacts (Section 5.3). The findings underscore the potential of multi-component analytical models in evaluating the mechanical performance of both new and existing systems, as discussed in Section 6, where future developments are also outlined.

2. Methodology

As defined in EAD 340059-00-0106 (2018), rockfall barriers are considered as protection kits, in which a set of components, slightly different among technologies and producers, are assembled. The interactions among them also depend on the specific barrier technology. To develop a comprehensive analytical model of the entire system, easily adaptable to different technologies and grounded in the product's assembly structure, a multi-scale approach was adopted. Each component was idealized using its own analytical mechanical representation, referred to as a subsystem in this work. The various subsystems were assembled into a system according to the way their real counterparts are assembled in the kit. This assembly of subsystems aims at replicating the structural load path leading to energy dissipation (Castro-Fresno et al., 2009).

For each subsystem, the resisting and energy-dissipating mechanisms were identified, along with the key variables that characterize these mechanisms. At the subsystem scale, the variables can be classified as either internal or external. Internal variables refer to geometrical (e.g., size, length), mechanical (e.g., strength, Young's modulus, Poisson's ratio), or physical quantities (e.g., friction coefficient) that are used to analytically describe the behaviour of the component. External variables are either kinematic (e.g., displacement, velocity, acceleration) or static (e.g., force, bending moment, torque) quantities that are transferred from other subsystems. The values of the internal variables should be calibrated based on the results of tests conducted on real components. A set of mathematical expressions involving both internal and external variables was assigned to each component. These equations provide an analytical description of the mechanisms that arise within the component and their validity was verified using test results available in the literature, when available. When not available, numerical modelling was considered.

The assembly process consisted of defining the links between the subsystems according to their connections and the load transfer path. Fig. 2 illustrates the identified subsystems, the associated variables (internal and external), and the interactions among them. The red external variables relate to critical quantities that can compromise the capacity of the entire system. The flowchart mirrors the functioning of a real rockfall barrier. In the following, after highlighting the assumptions behind the development of the model (Section 2.1), the involved subsystems are mathematically described (Section 3) and their assembly is discussed (Section 4). Refer to the referencing reported in Fig. 2 to redirect to each subsystem.

2.1. Modelling assumptions and validity

The introduction of a set of simplifying assumptions is needed as the aim of the work is to develop a simplified and computationally efficient simulation method. To provide meaningful insights into its

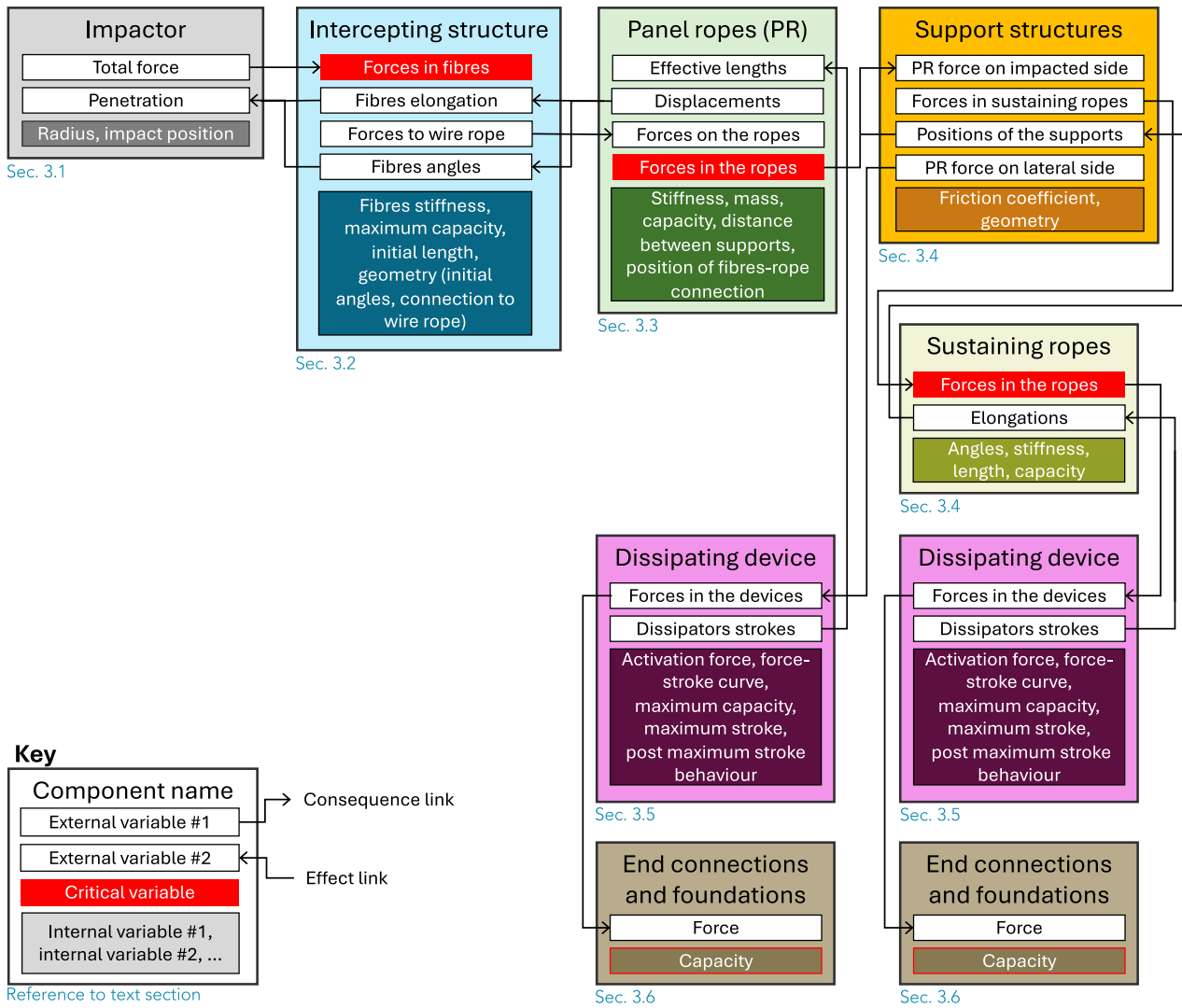


Fig. 2. Identification of subsystems, with detailed characterization of relevant variables and their interrelations. PR stands for “Panel Rope”.

suitability for assessing generic impacts, the model was validated for a specific rockfall barrier over a broad impact area, with comparisons of static, kinematic and energetic unknowns. For each component, the outputs of the analytical model were compared to the results of numerical simulations and, where available, experimental tests. The validation is limited to impacts on the net panels, excluding those on the supporting posts. The authors have evaluated impacts on supporting posts using finite element methods (Pimpinella et al., 2024b), involving simulations on HEA 120 steel posts made from S355 steel, with incident energies E_i ranging from 180 to 1000 kJ. Results have indicated that this impact condition can compromise the residual height of the system, a key performance parameter which may fall below the threshold defined by EAD 340059-00-0106 (2018). Furthermore, the complete post failure, which did not occurred in the simulations, cannot be ruled out for higher E_i due to lack of experimental data. Nevertheless, the limited geometrical extension of the posts area compared to the entire system allows to neglect this load scenario. Validation is also restricted to the specific considered technology; for other types of flexible rockfall barriers, each component (e.g. intercepting structures differing from the widely used ring net) must first be identified, and any additional subsystems must be validated (if not already documented in the literature) before the model application.

Although the model generally accounts for the dynamic mechanical behaviour of the various flexible rockfall barrier components, the approach employed is based on quasi-static concepts, as justified by the

following considerations. The impact of the block against the barrier is a dynamic phenomenon, as strong accelerations are experienced by the rock block and barrier components. The system impactor-barrier can be thought of as a two degrees-of-freedom system: one body representing the impactor of mass m_i , and the other representing the impacted net fence. The two bodies interact through a non-linear contact force. The barrier undergoes large displacements, which are controlled by the compliance law of a force acting where the block impacts. The mass of the body representing the net fence, M_B , does not correspond to the total mass of the barrier. Instead, it is the sum of the unit masses participating in the motion, weighted based on their displacements. Since only the net experiences the largest motion, the participating mass is small compared to that of the impactor (i.e., $M_{B,p} \ll m_{i,p}$). For this reason, when the impact occurs, the behaviour of the impactor can be described neglecting the inertia of the barrier. Recalling energy conservation, further discussed in Section 4.1, the kinetic energy is dissipated through elastic and permanent deformations, which are determined through the compliance law previously defined. Hence, it is possible to study the behaviour of the system in a quasi-static manner as the contribution of the inertia of the impacted system is peripheral in the equations of motion. This assumption also holds because the model is intended to evaluate the ultimate state of flexible rockfall barriers, typically reached with large impactor masses. This approach aligns with certification procedures, where bullet effects, which involve

net inertia (Cazzani et al., 2002; Spadari et al., 2011; Dhakal et al., 2012; Mentani et al., 2015), are neglected. In practice, bullet effects are mitigated by adding a secondary intercepting structures (e.g., hexagonal meshes) with smaller openings in the assembly (Volkwein et al., 2009).

Other assumptions are related to the impact direction, simulated as perpendicular to the intercepting plane in the model, and to the impacting kinetic energy nature, considered as purely translational. Rotational kinetic energy has a negative effect on the main components of the barrier (Qi et al., 2018a), but a pioneering experimental work involving impacts performed on a natural slope and a vertical drop test site has demonstrated that the effects caused by the impactor rotation can be reproduced with the execution of eccentric impacts (Caviezol et al., 2022).

The analytical model assumes a planar contact surface between the impactor and the net. That said, the model does not explicitly resolve the contact through mechanical interaction. Instead, it uses a kinematic constraint to identify the fibres engaged during the impact and to enforce appropriate restrictions on their motion. This modelling choice is justified by the fact that failures typically initiate in the vicinity of the contact area, rather than precisely at the contact interface (Xu et al., 2018b). Even though this simplification may be unreliable for impactors with excessively sharp edges, which could cause local damage to the net and potentially compromise its continuity, it remains appropriate in most cases and consistent with rockfall barrier certification procedures.

The impactor deviation occurring in case of eccentric impacts, which is beneficial for the barrier behaviour (Zhao et al., 2020), is only partially taken into account. This phenomenon is mainly due to two factors: (i) the requirement to satisfy the equilibrium equations in all directions at each step, and (ii) the differential activation of dissipating devices installed on opposite sides of the panel wire ropes. The former was neglected in the model, since numerical simulations of isolated net panels subjected to an incoming energy of 1000 kJ (Pimpinella et al., 2025) have shown only a limited deviation of the impactor under realistic dynamic impact conditions. The latter, instead, is explicitly accounted for in the model.

The friction phenomena occurring during the impact between the intercepting structure and panel wire ropes are not explicitly taken into account in the model. As shown in Coulibaly et al. (2018), these phenomena can have a significant effect on the rope deflection, while the force at the rope supports and the consequent activation of dissipating devices are only slightly affected.

3. Model subsystems

3.1. Impactor

Since the enabled approach is based on quasi-static concepts, only the contact shape between the impactor and the net is modelled, without introducing the impactor velocity inside the computation. Hence, the internal variables are the radius R and the position of the impact, namely, the eccentricities e_X and e_Y . In the model, the increase in the imposed force at the impactor-net contact points is transferred by net fibres to panel ropes, causing their deflection and resulting in an increase in the impactor displacement w in the Z -direction. The external variables are, thus, the position of the impactor and the sum of the forces acting on it.

3.2. Intercepting structure

The subsystem of the intercepting structure is responsible for linking the action exerted by the impactor to the response of the panel wire ropes, in terms of both forces and displacements. The intercepting structure is modelled as a single continuous panel spanning the entire

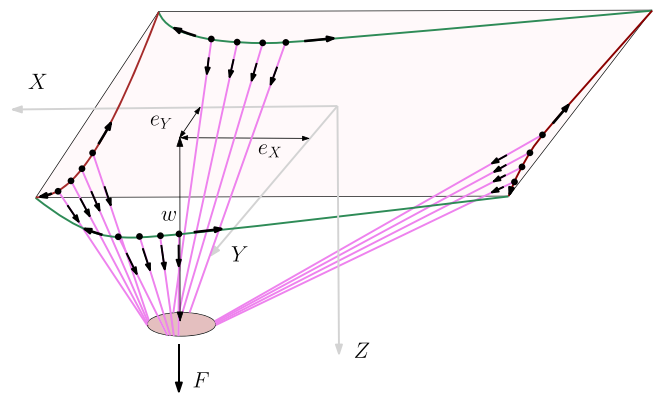


Fig. 3. Representation of a generic net panel with flexible boundaries. The reference system XYZ is located at the centre of the panel. When an impact occurs at the generic position described by the eccentricities e_X and e_Y , the penetration of the impactor (shown in pink) loads the component. The equivalent fibres (pink), connected to the panel's wire ropes at known coordinates (black dots) progressively stretch and absorb loads (black arrows). These loads are then transferred to panel wire ropes, which are responsible for transmitting them to the other components of the system.

barrier, regardless of the number of modules. From this point forward, this portion is referred to as the panel.

The equivalent fibre approach proposed by Guo et al. (2020, 2022), originally developed for ring net intercepting structures, was selected as the most suitable method for modelling flexible panels (membranes). In accordance with the quasi-static punching tests recommended by ISO 17745 (2016) for characterizing net performance, in this approach the impactor is idealized as a punching element with a diameter equal to the equivalent diameter of the actual impactor. Thus, the dynamic impact is modelled as an imposed force at the impactor-panel contact points. In the subsystem of the intercepting element herein adopted the definition of the geometrical and mechanical properties of the equivalent fibres are based on original formulation by Guo et al. (2020, 2022), while some important improvements have been previously made by the Authors, as reported in Pimpinella et al. (2025). Fig. 3 reports a sketch of the panel. A XYZ reference system is positioned in the centre of the panel. The coordinates of the impact are denoted as e_X and e_Y , while the position of the impactor, which moves along the Z -direction, is denoted as w . The contact points between the net and the impactor's edge define one end of the fibres, with coordinates determined by the geometry of the rings in the case of a ring net and the panel aspect ratio. For mesh panels (e.g., rhomboidal or hexagonal), the number of fibres does not coincide with the number of contact points due to the high mesh density. In such cases, the number of fibres can be reduced based on the impactor size and mesh spacing. The positions of the force application points on the panel ropes are determined to account for the wire rope-to-net connections in flexible systems, which allow the ring chains to migrate closer to the impact location. Consequently, the attachment points of the fibres to the panel wire ropes are defined within a specific region of the ropes, namely, in the vicinity of the impact zone, extending over a length equal to three times the impactor diameter. This initial choice, supported by experimental observations, has already proven effective for isolated ring net panels (Pimpinella et al., 2025) and is herein extended to the entire system.

Notably, this model of the net is also applicable to other configurations, such as drapery meshes (Marchelli et al., 2023), by calibrating the force-displacement curve parameters using standardized quasi-static tests (ISO 17745, 2016). However, the load transmission mechanisms of interception systems that differ from the widely used ring-net solution should be thoroughly investigated, especially when considering the extension of the generalized multi-component analytical model to such

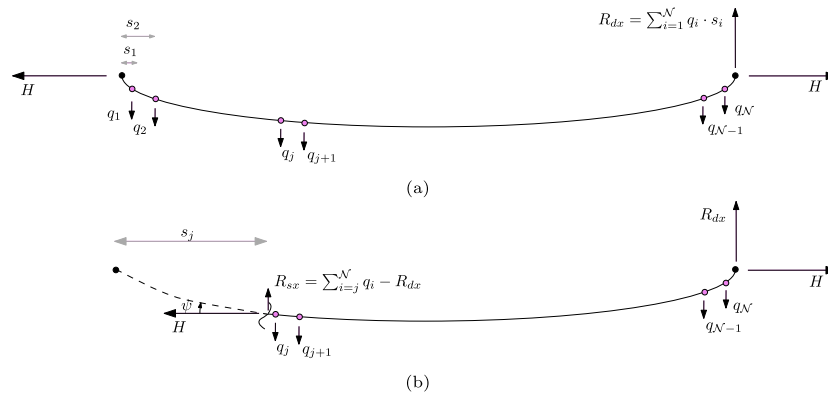


Fig. 5. Concentrated forces $q_{1,\dots,N}$ acting on the panel wire rope (a) and j th element equilibrium (b). The concentrated forces comprehend the dead load and the forces transmitted by the net fibres.

Considering a line coordinate s along the rope (measured along the line connecting its two support points), the external displacement $v(s)$ and the axial force T_i at the rope supports can be determined following the procedure described below. The rope is discretized into equally spaced segments, each with the same self-weight and length. Additionally, the loads from the fibres, denoted as Q , are applied on the rope at their specific positions (Fig. 5), fixed during the computation, as the sliding between the net and panel wire ropes is not taken into account in the model (Section 2.1). A total of N forces, named as q for sake of clarity, acts on the rope. Given an initial estimate of the horizontal support force H , acting in the direction of the undeformed rope, the displacement of each segment and the positions of the applied loads are computed using equilibrium equations, resulting in the rope's line of thrust. This is done by calculating the vertical reaction force R_{dx} on the right-hand side support and progressively recomputing the internal force as shown in Fig. 5. The direction ψ of the rope is determined as:

$$\psi = \arctan \frac{\sum_j^N q_i - R_{dx}}{H} \quad (3)$$

Based on the deformed configuration, the total rope length ℓ_t (defined as the cable length between the nearest external restraints) is calculated and compared with the length estimated from the average axial force \bar{T} , using the rope's elastic modulus and area A . The value of H is then refined iteratively until the discrepancy in the total length becomes negligible. In mathematical terms, the problem can be rewritten as:

$$\min_H \left[\ell_0 + \frac{\bar{T}}{E_{eq}A} \ell_0 \right] - \ell_t(H) \quad (4)$$

The optimization was performed using the Nelder–Mead Simplex method (Nelder and Mead, 1965), a well-established derivative-free optimization technique. The axial forces acting at both ends of the panel ropes are transferred to the support structure.

3.4. Support structure

The support structure, consisting on the posts and their foundations, sustains the panel ropes and, hence, the intercepting system. Sustaining (upslope and lateral) ropes are connected to the top ends of the posts to prevent its overturning in all the directions. The panel ropes are free to move on the support structure ends through mechanical devices that constrain their position. In moving, a friction force T_{μ} , equal to:

$$T_{\mu} = T_i (1 - e^{-\mu\theta}) \quad (5)$$

arises, where T_i is the force acting on the panel rope on the impacted side of the support, μ is the dynamic friction coefficient, and θ is the difference between the directions of rope axes on the two sides of the

support structure (Fig. 6). Assuming a circular shape for rope guides, the axial force corresponding to the not-impacted (lateral) side of the support, T_l , can be estimated with the Euler–Eytelwein formula as:

$$T_l = T_i e^{-\mu\theta} \quad (6)$$

A successive application of the equation enables the determination of the axial force at the terminal side of the barrier, denoted as T_r . The quantification of the friction coefficient between surfaces under dynamic conditions, denoted as μ , is a non-trivial task. It is strongly influenced by local conditions and the design of the sliding surfaces, which are closely tied to the specific technology employed. For example, a low friction coefficient may be expected if surface treatments, such as lubrication, are applied to the post heads and rope surfaces. Moreover, the friction coefficient can vary with contact pressure: at low contact pressures, the formation of superficial oxides may occur, whereas high contact pressures can lead to local plastic deformations (Blau, 2008).

For equilibrium of the posts' heads, the vectorial difference between T_l and T_i is transferred to the upslope ropes. Fig. 6 depicts the forces acting on the support structure. To clarify the naming of the forces, three subscript letters are adopted: the first letter denotes the side, either internal (impacted) i or lateral l ; the second letter refers to the post, e.g., post j ; the third letter defines the rope, e.g., u upper panel rope, s sustaining rope, l lower rope. Referring to Fig. 6, the Z-component of the maximum forces in the upslope (sustaining) ropes on the j th post, $T_{max,j,s}^Z = \max(T_{l,j,s}^Z, T_{i,j,s}^Z)$, is computed as:

$$T_{max,j,s}^Z = \frac{1}{2} \gamma T_{i,j,u}^Z \quad (7)$$

where $T_{i,j,u}^Z$ is the Z-component of the force in the upslope rope of the impacted module, while γ is an uneven load distribution factor, which serves to consider that forces are not evenly split between coupled upslope wire ropes, based on Eq. (7). In general, the value of γ can be determined from the results of experimental tests or numerical models.

The force $T_{max,s}$ is, then, reprojected along the direction of the rope, as:

$$T_{max,s} = \frac{T_{max,s}^Z}{n^Z} \quad (8)$$

where n^Z is the Z-component of the direction cosine of the rope. Notably, when dissipating devices are also installed on the sustaining ropes, their activation induces an elongation of the rope itself and a displacement of the unconstrained end of the steel post (Fig. 6(b)). In barriers which adopt dissipating devices on the sustaining ropes, the related post is connected to the base plate via a spherical hinge, allowing it to reorient while maintaining tension in both attached upslope ropes in case of activation of the dissipating devices. An iterative procedure is, thus, needed to estimate the static unknowns, since the activation of

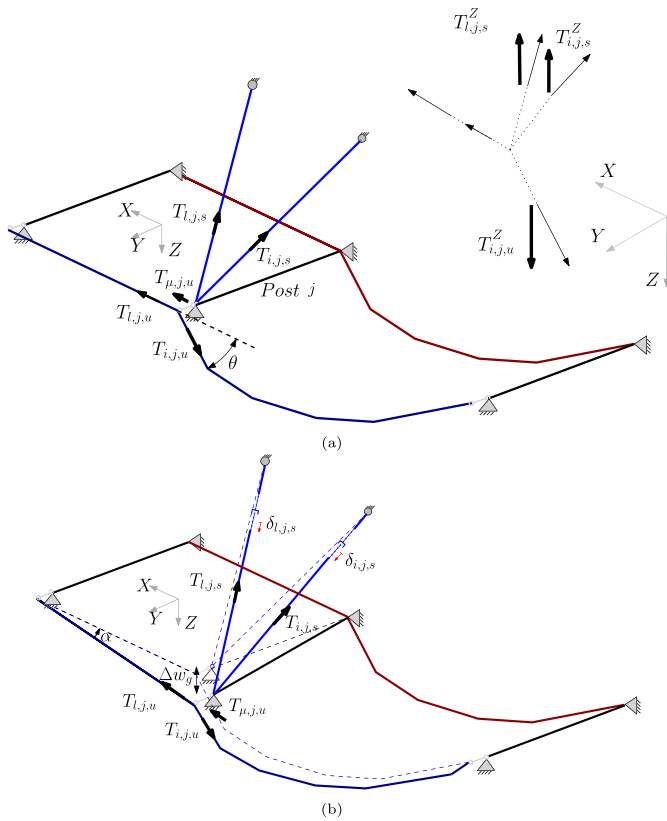


Fig. 6. Post head equilibrium of forces in absence (a) or presence (b) of dissipating devices, as it can happen in specific barrier models.

dissipating devices modifies the geometry and, as a consequence, the subsystem’s equilibrium. The post-activation kinematics of a generic steel post equipped with upslope dissipating devices is well described in Yu et al. (2018), whose equations governing this behaviour were adopted in the present work. The post head downward displacement Δw_j can thus be estimated. The consequently modified geometrical configuration of the panel wire rope (due to the downward displacement of one of its supports) is taken into account in the model assembly.

The internal parameters are the friction coefficient rope-post, while the external parameters are the axial forces in all the ropes and the position of the support.

3.5. Dissipating devices

The subsystem consists of mechanical devices that are activated when the force in the rope reaches a specific threshold. These devices dissipate energy through friction and/or material deformation. During the dissipation process, the distance between two arbitrary points, one located on the ground anchor rope and the other on the active rope, both external to the dissipating device, increases. This increase in distance is referred to as the stroke. The external variables governing the system are the force transmitted through the connected ropes B , estimated in the model as the wire rope force at the rope connection with the device, and its stroke δ . The internal variables include the shape of the force-stroke curve and its defining parameters.

The relationship between the force at the ends of the dissipating device, B , and its elongation is generally described by a trilinear curve (Fig. 7). The first segment corresponds to the elastic loading phase, extending from zero up to the activation force, B_a . The second segment represents the stroke of the device, during which irreversible

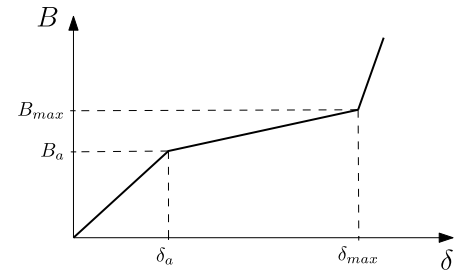


Fig. 7. Typical force–displacement behaviour for an dissipating device used in rockfall barriers.

displacement occurs under a nearly constant force, up to the maximum elongation, δ_{max} . The third segment begins at the maximum elongation and characterizes the response of the system once the designed dissipating mechanism is fully exploited. The specific dissipating device technology can show a stiffer response or break after δ_{max} is reached. In these two cases, the device is respectively modelled as a rigid component or as a failed element with null residual capacity, causing a condition which is equivalent to the failure of the connected rope. The integral of the force over the stroke is the energy dissipated in the device, called E_b .

In general, the force–displacement behaviour can be determined through quasi-static experimental tests (Escallón et al., 2014; Xu et al., 2018a), dynamic numerical models calibrated using quasi-static data (Gentilini et al., 2013), or, when available, dynamic experimental tests (Fulde and Müller, 2013; Castanon-Jano et al., 2017, 2019). Although dynamic tests provide a more accurate representation of real impact conditions (Trad et al., 2013; Qi et al., 2018c), they are not always accessible. In a previous study, Pimpinella et al. (2024a) conducted an in-depth investigation into the mechanical behaviour of energy dissipating devices. For several commonly used technologies, analytical models were proposed and calibrated using quasi-static test results. This approach is considered appropriate, as for most technologies, the post-activation phase exhibits similar trends under both static and dynamic conditions. The activation force B_a is typically the only parameter significantly influenced by the dynamic nature of the loading process (Osairan et al., 2025).

3.6. End connections and foundations

End connections and foundations represent the last part of the load-transfer process. The external variables associated to this subsystem are the force from the ropes and the capacity. Briefly, a ultimate capacity U_{max} of the connection, related either to the end connections or to the foundations, can be assigned. Failure occurs when this capacity is exceeded by the force in the wire rope measured at the ground anchor, named T .

4. Model assembly and calibration

The concepts herein proposed for the analytical model can be implemented into a system with an arbitrary number of modules. As an example, Fig. 8 depicts the scheme of a generic three-modules rockfall barrier. In the model, the applied force at the impactor-net contact points is transmitted through the net fibres to the panel ropes, causing their deflection and increasing the impactor’s out-of-plane displacement, w . In Fig. 8(a), the forces transmitted by equivalent fibres are indicated with the letter N and subscripts which denote the progressive fibre number (from 1 to n for the fibres connected to the longitudinal ropes and from 1 to m for those connected to the transversal ropes) and the related wire rope (ul and ll for the upper and lower longitudinal ropes, while rt and lt for the right and left-hand sides transversal

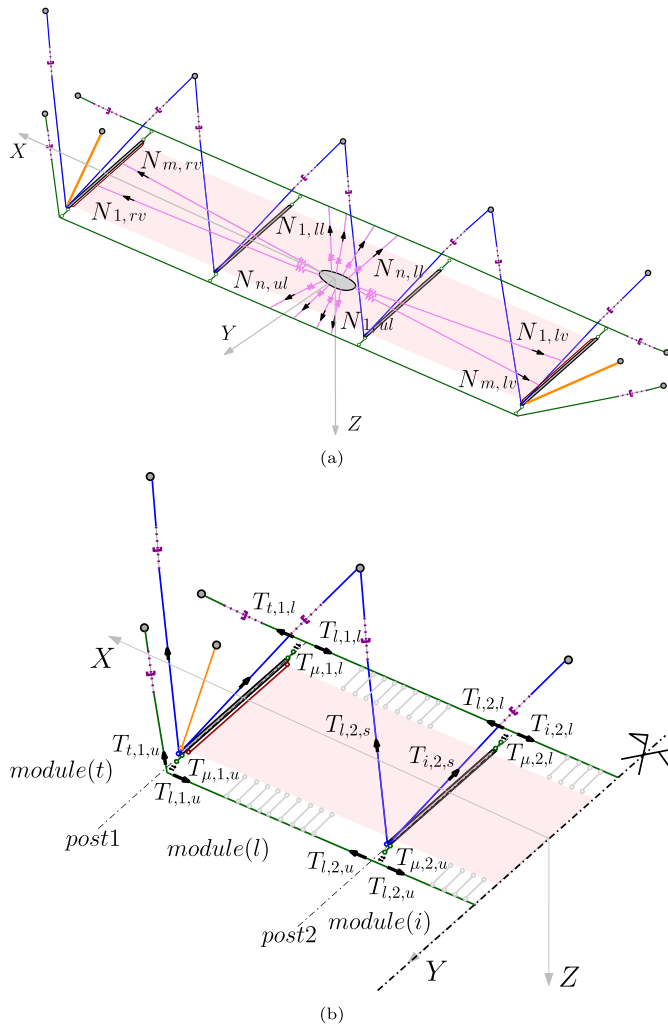


Fig. 8. Scheme of forces calculated in the analytical model in a generic flexible rockfall barrier: forces transmitted by the equivalent net fibres (a) and wire rope cables (b) forces.

ropes). These forces are transferred to panel ropes, i.e. longitudinal and transversal ones, and to the upslope sustaining ropes, whose force is expressed with T and a subscript coding described in Section 3.4 (Fig. 8(b)). In real-world installations, lateral and potential downslope wire ropes play a crucial role in maintaining system stability. Despite their structural importance, these components are excluded from the analytical model, as their involvement in the energy dissipation process is minimal. Conversely, panel wire ropes are primarily responsible for transferring loads to the rest of the system, including the dissipating devices. When the tensile force in a wire rope exceeds the activation threshold of the corresponding dissipating device (B_a), its mechanism is triggered. This not only initiates energy dissipation but also contributes additional flexibility to the system as the length of the rope between the supports increases.

For each impact position, the mechanical behaviour of the entire system can be defined by analysing and combining four substructures. These substructures correspond to the four mechanical regions loaded by the net during an impact event (depicted in different colours in Fig. 9). Each substructure includes the complete set of subsystems shown in Fig. 2. Exceptions are the sustaining ropes and the related dissipating devices and foundations, which are present in the upper longitudinal substructure, only. The length variation of longitudinal wire ropes due to the activation of dissipating devices is considered within

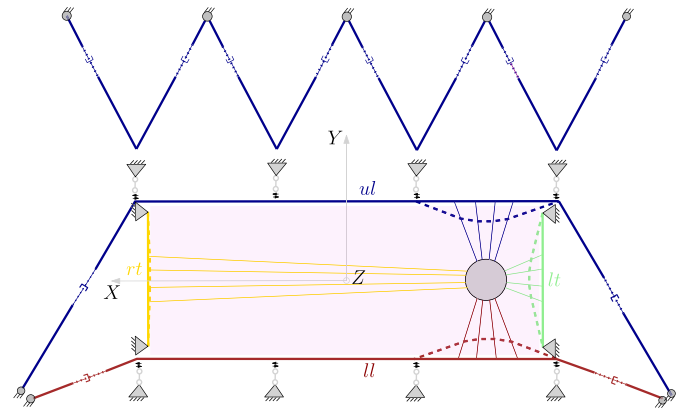


Fig. 9. Representative scheme of longitudinal and transversal substructures.

the analytical calculations of longitudinal substructures. As stated in Section 2.1, the model does not account for sliding between the net and the connected wire ropes. However, in the computation, the panel ropes can move due to the differential activation of dissipating devices installed on its opposite sides, causing a consequential movement of the connected equivalent fibres.

Since energy dissipating devices are typically not installed on transversal ropes, the amount of energy dissipated through transversal substructures is usually reduced. Nevertheless, transversal substructures can still lead to failure. The absence of dissipating devices makes these substructures less flexible and prone to failure especially in the case of impacts on the lateral modules of the barrier. In this case, the shortest and consequently stiffest and most loaded fibres in the mechanical assembly can belong to transversal substructures.

The method implicitly accounts for the concept that, during the loading phase, mesh deformation tends to divert loads towards the longitudinal cables (Pol et al., 2021b). Indeed, fibres are always defined for all the four substructures, but the longest fibres are less stiff, consequently bearing a negligible amount of load if compared to the shortest ones.

The flowchart of the multi-step procedure applied to a generic substructure is presented in Fig. 10. By repeating this process for all four substructures and combining the results, the overall behaviour of the complete model is obtained. As shown, each substructure consists of several subsystems illustrated in Fig. 2. The input features consist in the properties of equivalent fibres, wire rope and, if present, dissipating devices connected to the rope. The process starts estimating the initial rope deflection $v(s)$, and the initial impactor position w_0 . This quantity ideally represents the minimum displacement which stresses the substructure, considering an initial relaxation of the intercepting structure. Then, fibres lengths and stiffnesses L and k can be estimated, being known their force–displacement behaviour. At that point, the algorithm starts to reproduce a force-controlled test, in which the force F is gradually applied to the impactor in the Z direction. At each step p , an increase in force ΔF is applied and the substructure response is estimated with an iterative procedure. The total force $F(p)$ is equal to ΔF multiplied by $(p - 1)$. At every iteration j , the applied force is redistributed to the fibres according to Eq. (1). Based on the geometry of the fibres, the forces Q acting on the rope are computed according to Eq. (2). Then, $T(s)$ and $v(s)$ are calculated according to the procedure reported in Section 3.3, leading to a new estimation of length L and secant stiffness k of each fibre, and the impactor position $w_j(p)$. The process is repeated as the force is redistributed according the secant stiffnesses of the previous force step. When the difference between $w_j(p)$ and $w_{j-1}(p)$ becomes lower than 1 mm, the iterative process stops and the substructure stiffness $K_s(p)$ is estimated as:

$$K_s(p) = \frac{\Delta F}{\Delta w(p)}. \tag{9}$$

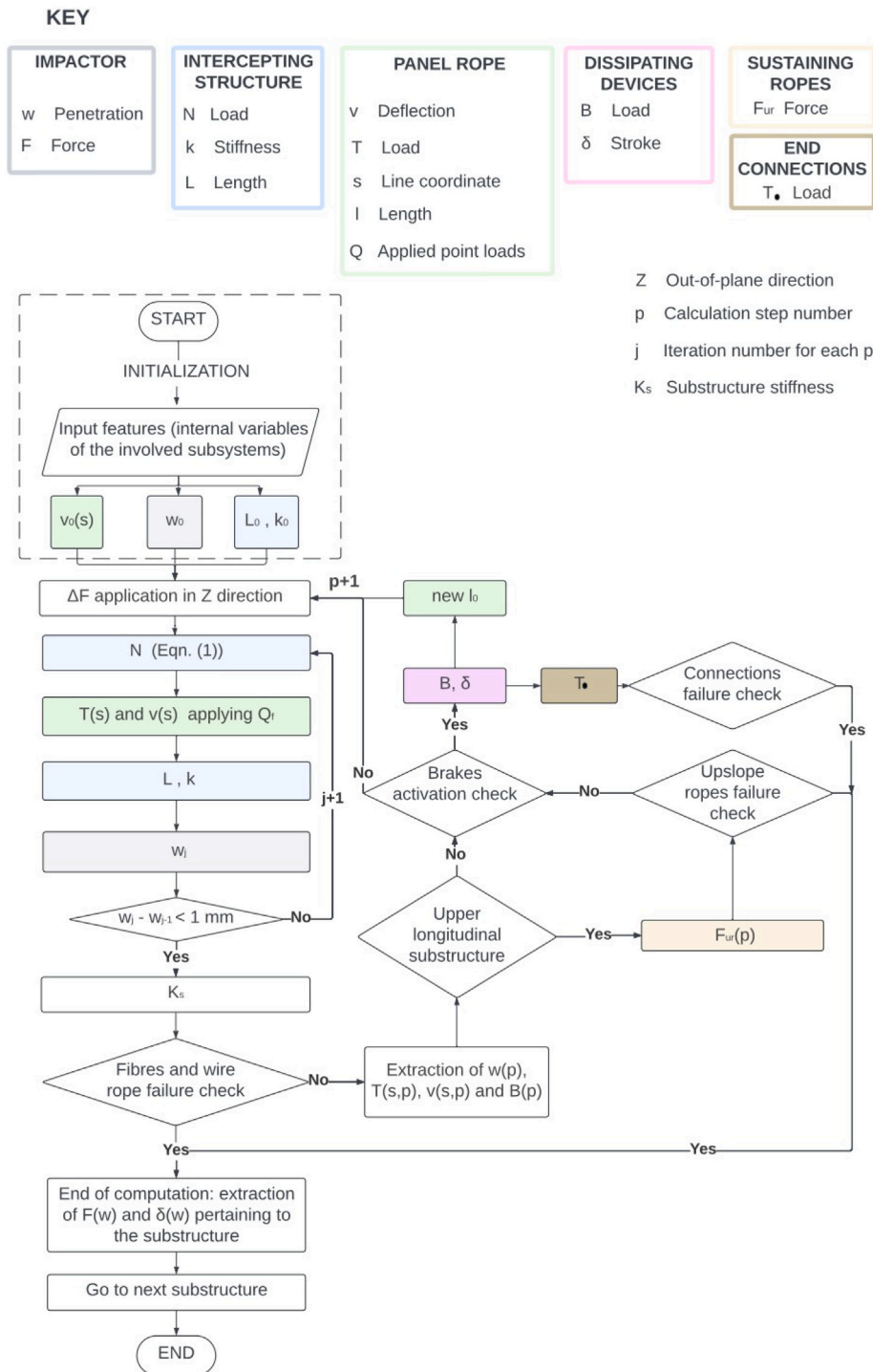


Fig. 10. Computation process for each substructure.

After verifying the absence of fibre or rope failures, the values $w(p)$, $T(s, p)$, and $v(s, p)$ are extracted, and the activation of dissipating devices is assessed by checking whether $B(t) \geq B_a$. The wire rope length $\ell(p)$ is incremented at every loading step of the sum of the strokes $\delta(p) - \delta(p-1)$ of each dissipating device. In case of activation on upslope ropes, at each loading step the forces applied on the panel rope are projected in the direction perpendicular to the chord which connects the two ends of the rope. The process continues by increasing the force step p . The computation is halted when failure occurs at a given step. The complete $F - w$ response of the substructure up to the point of failure is thus obtained.

Failure occurs if any of the following conditions is met:

- the forces in adjacent equivalent fibres exceed the corresponding capacities. The number of involved fibres is determined from the diameter of the impactor and the spacing between impactor-net contact points;
- the breaking force of a breakage-prone dissipating device is exceeded;
- the breaking force in any rope is exceeded;
- the breaking force in any rope end termination is exceeded.

These failure conditions correspond to the critical variables highlighted in red in Fig. 2. When one substructure fails, the computation for all the others is halted and outputs from all four substructures are extracted and combined by summation. The area below the $F-w$ curve represents the energy dissipated by the s th substructure according to the analytical model as:

$$E_{as} = (p) = \int_0^{w_{max}} F(w) dw. \quad (10)$$

Knowing the dissipating devices elongations $\delta(p)$, the fraction of energy dissipated by these devices at each step $E_{b,as}(p)$ is determined. The remaining portion of dissipated energy is further subdivided in energy dissipated by the intercepting structure plastic deformation and elastic energy stored by the wire ropes, as detailed in Section 4.1. By properly combining the results for the subsystem, the relationship between the force acting on the impactor and its position can be determined.

It is worth highlighting that the analytical model cannot account for all the contributions to energy dissipation that actually occur in a dynamic impact. The estimation of the total energy consumption using the proposed global analytical model is discussed in the following Sections (Sections 4.1 and 5.3), examining the energy balance and its implications for our case study.

4.1. Energy balance for flexible rockfall barriers

Differently from debris flows, where a significant portion of the energy is dissipated through the landslide internal energy (Zhao et al., 2022b), for rockfalls, the entire incoming energy has to be dissipated through the components of flexible rockfall barriers. As said, to be certified and put on the market, rockfall barriers are subjected to full-scale impact tests, in which their energy absorption is evaluated. Defined E_i as the incident kinetic energy for the test, i.e. when the impactor reaches the barrier position, this value is assumed to be equal to the nominal energy absorption capacity E_N for which the system is certified, provided that the impactor is stopped and the system's deformation requirements are met. Defined α the impact angle (i.e., the angle between the impactor's trajectory and the direction of gravity), w the net elongation, and $F(\zeta)$ the interaction force between the impactor and the system, it could be stated that:

$$E_{tot}(w) = E_N + m_i g \cos(\alpha) w = \int_0^w F(\zeta) d\zeta + E_{ks}(w), \quad (11)$$

where E_{ks} is the kinetic energy due to the movements of the whole structure. From Eq. (11) it is evident that the energy absorbed by the structure in a generic impact is actually higher than $E_i = E_N$. During the penetration, the impactor gradually loses an additional fraction of potential energy, which is transferred to the barrier. Therefore, the total consumed energy is evaluated at the failure time (in case of impact occurring along the direction of gravity) as:

$$E_{tot}(w_{max}) = E_N + m_i g w_{max} = \int_0^{w_{max}} F(\zeta) d\zeta + E_{ks}(w_{max}), \quad (12)$$

when the impactor ideally has zero velocity and the system reaches its maximum elongation w_{max} , while a fraction of kinetic energy $E_{ks}(w_{max})$ is still present, due to vibrations of the barrier components. Eq. (12) accounts for the fact that the impact (simulated either numerically or analytically) acts along the direction Z , perpendicular to the protective screen.

The area below the force–displacement curve of the dynamic impact represents the dominant part of the converted energy. This area consists of the internal energy of the barrier components E_{int} and the energy dissipated through sliding movements between parts and viscous processes, named E_{fd} and E_{vd} . E_{int} includes the energy dissipated by the components' plastic deformation and the elastic energy stored in the entire structure, respectively named E_{pd} and E_e .

Such energy analyses are required to validate the analytical model with a numerical model that outputs the various energy contributions.

Hence, a comparison of the results in terms of dissipated energy obtained in real scale tests and in the numerical model was performed, according to:

$$E_{tot}(w_{max}) = E_N + m_i g w_{max} = E_{pd} + E_e + E_{fd} + E_{vd} + E_{ks}(w_{max}). \quad (13)$$

To consistently compare the energies, it should be noted that in the analytical model, the calculated area below the $F-w$ curve also comprehends a fraction of E_{fd} (whose computation is not trivial) due to the fact that the schematization with equivalent fibres already considers the friction phenomena produced by the sliding between the rings. As stated, the model also accounts for the friction between the longitudinal wire ropes and the guides on the posts terminations. The friction between the rings of the net and the clamps to connect them to the rope is neglected, and kinetic energy at the braking time cannot be tackled given the quasi-static nature of our model. Also E_{vd} , due to possible high localized stresses in certain areas of steel posts, is not considered in the analytical model, since steel posts are modelled as rigid components.

In the numerical model, instead, all the contributions to energy consumption can be addressed. Also in this case a portion of E_{fd} is calculated within E_{pd} .

4.2. Calibration and validation

The calibration of the internal parameters of each subsystem can be carried out using the results of tests conducted on the actual components, as detailed in the corresponding sections. The complete model should then be calibrated and validated using full-scale tests, through which the dissipated energy and the forces acting on the main components are recorded and compared with the outputs of the model. In particular, the calibration is necessary to accurately determine the factor γ , which accounts for the uneven load distribution at the head of the support structure (see Section 3.4), and λ , accounting for the energy dissipation not explicitly modelled, such as the friction phenomena occurring at the connection between the net and the panel wire rope, or localized stresses on the posts. The calibration is also required for the threshold values used in the iterative procedure for computing the displacement w , the magnitude of the force increment ΔF .

Validation should confirm that the total dissipated energy and its distribution among the components, as computed by the analytical model, reflect the actual behaviour observed in the tests in terms of forces in the dissipating devices and final displacement of the impactor. As the model was developed to investigate a wide range of impact conditions (e.g. eccentric impacts), this process should be carried out for several representative impact scenarios. In case in which full-scale tests are not available in sufficient number or data are not sufficient, a numerical model of the system could be developed. When full-scale tests are either insufficient in number or lack adequate data, a numerical model of the system may be developed. This model should be validated against the available full-scale test data. As with the physical barrier tests, the numerical model of dynamic impact should be applied to only a limited set of impact scenarios. Consequently, the analytical model serves to evaluate the full spectrum of possible impact conditions and can be readily adapted to various technologies.

5. Example of application

All the calibration and validation steps before reported were made tailoring the model for a specific barrier, i.e. RXI-100 by Geobruigg AG, of which the results of a full-scale impact test in a specific position is available.

Introduced to the market in the early 2000s, the RXI-100 is a system manufactured by the Swiss company Geobruigg AG and is commonly used in existing applications. The system is designed to absorb a maximum energy of 1000 kJ as certified in 2004 in accordance with the Swiss guidelines (Gerber, 2001). Certification involved an impact test

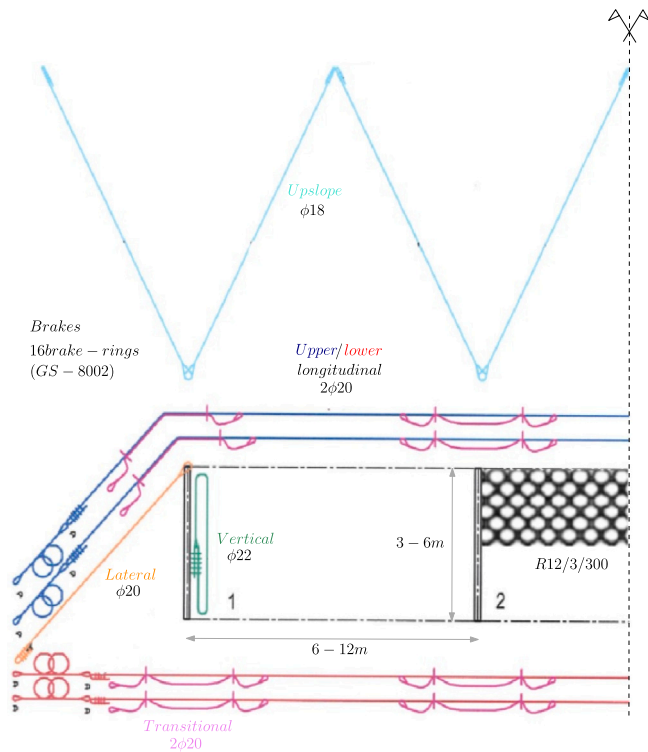


Fig. 11. Schematic of the RXI-100 flexible rockfall barrier system.



Fig. 12. Installation of the RXI-100 system during a full-scale test (image courtesy of Geobrugg AG).

at the centre of a central module within a three-module barrier, with a module spacing of 10 m and a system height of 4 m, as shown in Fig. 12. The intercepting structure consists of an R12/3/300 ring net, composed of rings with a diameter of 300 mm, each formed by 12 windings of high-strength steel wire with a diameter of 3 mm. The supporting structure is composed by HEB120 steel posts made of S355-grade steel. These posts serve as mounting points for the guides that hold the longitudinal wire ropes, which are duplicated in both the upper and lower positions. Each longitudinal rope is fitted with two GS-8002 brake rings on either side, resulting in a total of 16 energy-dissipating devices. To prevent load concentrations and maintain system flexibility, transitional ropes (shown in purple in Fig. 11) are installed adjacent to the posts.

Table 1

Summary of the internal variables of the analytical model of the RXI-100 barrier.

Subsystem	Description and reference
Intercepting structure	Trilinear curve for fibres determined through the following (force, elongation) points: (0,0), ($L_n, 0$), (1.1578 L_n , 9 kN), (1.1856 L_n , 110 kN) Guo et al. (2022) and Pimpinella et al. (2025)
Wire rope	Equivalent diameter 22 mm, $E_{eq} = 60$ GPa. Guo et al. (2022)
Support structure	Friction coefficient $\mu = 0.15$ Escallón et al. (2014)
Dissipating devices	Trilinear curve (Fig. 13) Qi et al. (2018c) and Pimpinella et al. (2024a)
End connections/foundations	Rigid element with unlimited capacity

It is worth recalling that the certification carried out in accordance with the Swiss guidelines (Gerber, 2001) differs from the procedure defined in EAD 340059-00-0106 (2018), as the Swiss method does not account for the initial sag of the system. This aspect is instead addressed by adjusting the experimental value of system elongation based on numerical results reported in Guo et al. (2024) for an isolated net panel with similar geometry.

5.1. Analytical model

The multi-component analytical model was implemented in Matlab (v.2025). Within the overall analytical framework, its subsystems were specifically calibrated to accurately represent the components of the RXI-100.

For the intercepting structure, the force–displacement curve available for the R12/3/300 ring net (Jin et al., 2021; Guo et al., 2022) was used to define the mechanical properties of the fibres. In the RXI-100 system, two longitudinal wire ropes are coupled; therefore, they are represented in the model by an equivalent rope connected to equivalent dissipating devices. The analytical model developed by Pimpinella et al. (2024a) can be adopted to describe the behaviour of the generic brake ring device. In this case, a force–stroke curve specific to the GS-8002 brake ring was available (Fig. 13). A comprehensive study by Qi et al. (2018c) has also investigated the mechanical behaviour of brake rings under dynamic loading, including configurations with series and parallel arrangements. These findings were used to refine the subsystem of dissipating devices, which are represented using a trilinear force–displacement curve consisting of a pseudo-elastic phase followed by two plastic domains. The primary load path involves the longitudinal substructures, comprising all dissipating devices connected to the longitudinal wire ropes. Table 1 summarizes the internal variables included in the analytical model of the RXI-100 barrier.

5.2. Numerical model

As only one full-scale impact test is available, a numerical model of a three-module barrier was developed to validate the analytical model for impact scenarios differing from the centred configuration specified in the Swiss guidelines. A finite element (FEM) model was created using the dynamic explicit environment in Abaqus (Abaqus/CAE v.2024).

Referring to the intercepting structure, although detailed models of the ring net can be constructed using beam elements with appropriate interaction properties (Escallón et al., 2014; Xu et al., 2018a; Qi et al., 2018b), such models require significant computational effort. Simplified approaches employing an equivalent membrane have proven to be a feasible alternative (Mentani et al., 2018; Jin et al., 2021), and this method was adopted in the present study. As a result, the net's behaviour (numerically plastic) is also influenced by the sliding that occurs between the rings. The net was therefore modelled as an

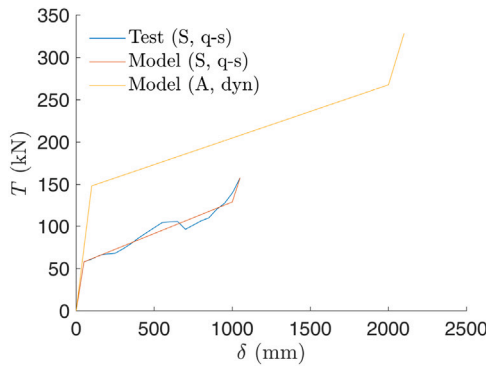


Fig. 13. Quasi-static and dynamic characterization of the GS-8002 brake ring. The single dissipating device (S) was tested and modelled under quasi-static (q-s) conditions, while the dynamic behaviour resulting from the actual series and parallel arrangement (A) of brake rings in the RXI-100 system is based on data from Qi et al. (2018c).

equivalent membrane, with dummy rigid elements introduced to provide flexibility and to connect the membrane to the panel wire ropes, as illustrated in Fig. 15. The parameters of the equivalent shell were derived from quasi-static punching tests (ISO 17745, 2016) conducted on a square panel with 3-m sides.

The wire ropes were modelled as one-dimensional elements. The panel steel wire ropes, which are subjected to out-of-plane loads, were represented using beam elements with reduced flexural inertia. Truss elements were employed for the remaining wire ropes, which are primarily subjected to axial dynamic loads. As previously mentioned, the mechanical properties of wire ropes differ significantly from those of a solid steel bar with the same nominal cross-sectional area. Unlike the analytical model, the numerical model uses the effective cross-sectional area rather than the nominal one, to more accurately capture the dynamic behaviour of the wire ropes. Accordingly, the equivalent elastic stiffness was set to 112 GPa (Escallón et al., 2014), accounting for the sliding between individual wires under load. Energy-dissipating devices were implemented using axial connectors, with the same force-displacement relationship adopted in the analytical model (see Fig. 13b).

The steel posts were modelled using interconnected shell elements, with material properties incorporating both hardening and damage phases. Specifically, a Cowper–Symonds power law was used to model strain rate-dependent hardening, while a Johnson–Cook damage model was applied to simulate failure, based on studies conducted on S355 steel (Forni et al., 2016; Ribeiro et al., 2016).

The dynamic friction coefficients for steel-to-steel and impactor-to-net contacts were assumed to be 0.1 and 0.4, respectively. Such values were determined from the literature studies on similar structures (Escallón et al., 2014; Jin et al., 2021).

The shape of the impactor used in the full-scale tests was accurately reproduced in the numerical model. This results in a non-planar contact surface with the intercepting structure. An equivalent diameter for the impactor is instead adopted in the analytical model, as illustrated in Fig. 14.

Regarding the mesh, the intercepting structure was discretized using 25 mm × 25 mm shell elements. The most computationally demanding components were the steel wire ropes, which were discretized with beam and truss elements at 5 mm intervals. This fine mesh was necessary to accurately model the connections with the steel net, resulting in a stable time increment of 9.11×10^{-7} s. The total simulation time was set to 0.3 s, with the impact occurring at the beginning of the simulation. Mass scaling was applied to the connecting components at the base of the posts, resulting in a total mass increase of less than 5% of the overall system mass (see Fig. 16).

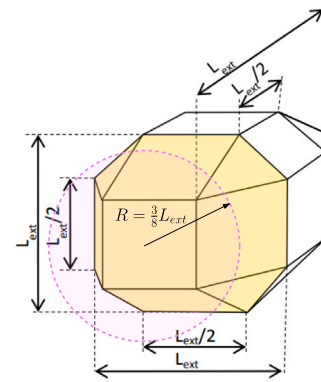


Fig. 14. Impactor to intercepting structure contact area.

5.3. Validation and discussion

Model validation was carried out for five different impact positions, which are schematically illustrated in Fig. 17. In the field test, corresponding to the centred impact position, maximum forces were measured during the experiment using load cells installed on the upslope and longitudinal ropes. Additionally, the final extension of all dissipating devices was recorded at the end of the test. This impact scenario was also simulated using the numerical model, and served to verify that the FEM model accurately reproduced the real-case behaviour. Impact positions 2 and 3 were selected to validate the analytical model under eccentric impact conditions along the Y direction, while eccentric impact conditions along the X direction are studied with impacting positions 4 and 5 (Fig. 17). For these cases, only the results from the numerical model are available. Simulations were performed on a workstation equipped with an Intel Xeon Silver 4214 CPU (2.2 GHz, 12 cores) and 24 GB of RAM. The total running time of the numerical simulations varied slightly across the different impact scenarios, with an average duration of 4.58 h. A similar trend was observed for the analytical simulations, which had an average running time of 0.08 h, corresponding to a 98% reduction in computational time.

Along with the impacting positions selected for the validation process, Fig. 17 represents longitudinal (green) and transitional (purple) ropes involved in the longitudinal substructures. As visible, the transitional ropes are not involved in the load path, except when the impact occurs in areas contiguous to one of the steel posts. Inside the model, in this latter case, the fibres belonging to longitudinal substructures are linked with an equivalent panel wire rope. This equivalent rope simulates the combined response of transitional and longitudinal wire ropes. Practically, an equivalent length of the panel wire rope, estimated after the observation of the deformed shape of the system in the numerical simulation (Fig. 18) is introduced inside the analytical model.

Given that dissipating devices account for the majority of the system's energy dissipation, several related parameters are introduced and considered in the validation. The mean extension of all dissipating devices is denoted as $\bar{\delta}$. Additionally, mean extensions are defined for the dissipating devices located in the right, left, upper, and lower half-planes of the system. Specifically, $\bar{\delta}_{X+}$ and $\bar{\delta}_{X-}$ represent the average extensions of the dissipating devices on the right and left sides of the system, respectively, while $\bar{\delta}_{Y+}$ and $\bar{\delta}_{Y-}$ correspond to those connected to the upper and lower wire ropes.

These values are used to assess the degree of asymmetry in the system's response. To quantify this, the asymmetry parameters Δ_X , Δ_Y , and Δ_{XY} are defined as follows:

$$\Delta_X = \frac{|\bar{\delta}_{X+} - \bar{\delta}_{X-}|}{\bar{\delta}_{X+} + \bar{\delta}_{X-}}, \tag{14}$$

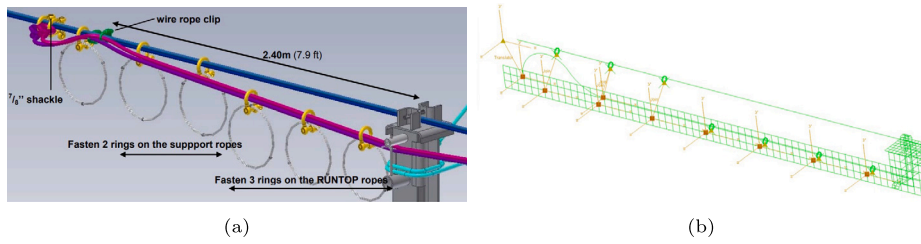


Fig. 15. Ring net to panel wire ropes connections in the real assembly (a) and in the numerical model (b).

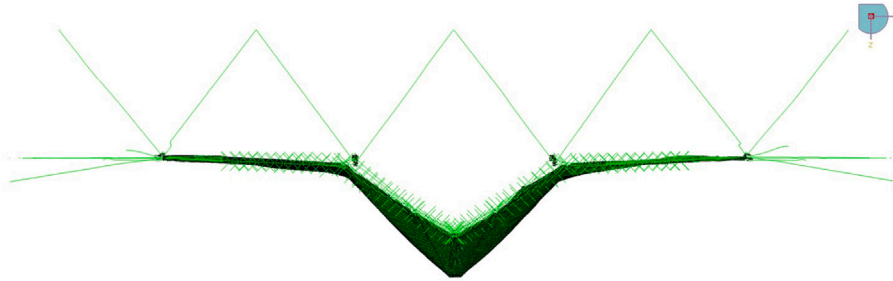


Fig. 16. Deformed geometry of the system (according to the numerical model) at braking time.

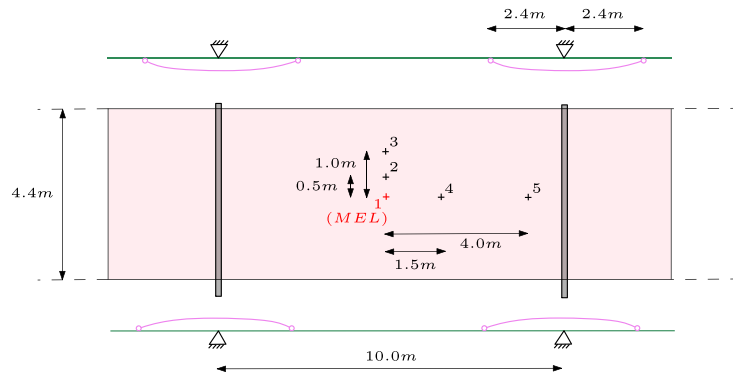


Fig. 17. Impact positions within the barrier central span for the analytical model validation.

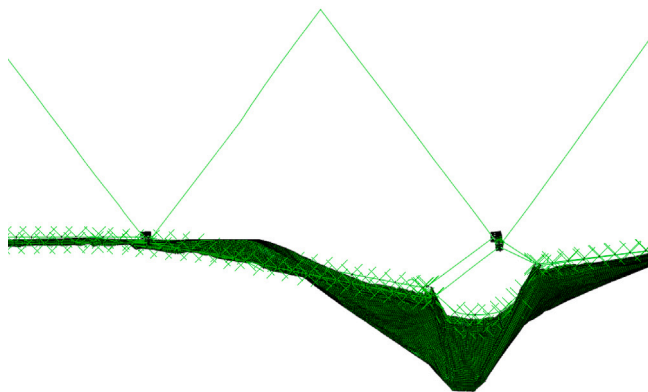


Fig. 18. Deformed shape at failure for RXI-100 under impacting position 5 ($e_x = 4.00$ m) in the numerical simulation.

$$\Delta_Y = \frac{|\overline{\delta_{Y+}} - \overline{\delta_{Y-}}|}{\overline{\delta_{Y+}} + \overline{\delta_{Y-}}}, \tag{15}$$

$$\Delta_{XY} = \sqrt{(\Delta_X)^2 + (\Delta_Y)^2}. \tag{16}$$

An increase in Δ_X and/or Δ_Y indicates that the system is more heavily loaded in the X and/or Y directions, respectively. These parameters range from 0, representing a completely symmetric response, to 1, indicating a fully asymmetric response in the respective direction. The parameter Δ_{XY} serves as a synthetic indicator of overall asymmetry. It takes a value of 0 in the case of a fully symmetric response in both directions, and reaches a maximum of $\sqrt{2}$ when the system exhibits complete asymmetry in both the X and Y directions.

To calibrate and then validate the analytical model, the results obtained are compared with numerical and experimental data for the centred impact scenario, and with numerical data only for the eccentric load cases. As highlighted in Section 4.1, the analytical model cannot account for all possible contributions to energy dissipation. Therefore, the comparison was used to determine the value of an energy amplification coefficient, λ , for the entire model. From our numerical model on RXI-100, it results that the ratio between the internal energy and the

Table 2
Analytical model validation for centred MEL impact.

Output ($\bar{\lambda}, \bar{\eta}, \bar{\gamma}$)	Running time (h)	E_{tot} (kJ)	w_{max} (mm)	$\bar{\delta}$ (mm)	E_b (kJ)	E_n (kJ)	$T_{max,l}$ (kN)	$T_{max,s}$ (kN)	Δ_X (-)	Δ_Y (-)
Test	-	1166	5300 ^a	1030	713.3 ^b	-	230	135	0.01	0.03
Num	4.72	1175	5584	980.7	694.2	242.0	210.3	150.1	0.01	0.10
Anal	0.04	1182	5795	1080.3	779.9	223.7	234.2	113.8	0	0

^a Adjusted with the initial sag reported in Guo et al. (2024).

^b Derived from the measured dissipating devices strokes (Gerber, 2001).

total energy consumed by the barrier (E_{int}/E_{tot}) is on average equal to 0.853. This finding is consistent with the results reported by Xu et al. (2018a), who have found that for a different technology designed to withstand impact energies ranging from 750 kJ to 5000 kJ, the ratio E_{int}/E_{tot} was on average equal to 0.780. This is also coherent since in our numerical model a portion of the frictional energy dissipation derives from as plastic energy dissipation in the net, given the membrane approach used for the net. Based on this, a reasonably accurate value of λ , derived by evaluating the share of energy associated with frictional and kinetic mechanisms in a numerical model, is obtained and is equal to 1.17 ± 0.02 . With λ , the energetic effects, which are not directly considered in the model, are smeared over the entire structure, introducing a simplification that enables a more tractable global analysis. Similarly, the coefficient γ introduced in Section 3.4 to consider the uneven loading of supporting ropes, was calibrated and set equal to 1.19 ± 0.08 by minimizing the discrepancy between the results provided by the numerical model and the available experimental test.

Table 2 presents a comparison among the experimental, numerical, and analytical results for the centred impact scenario. The comparison includes system elongation, energy dissipation distribution, and the maximum forces in both the longitudinal and sustaining wire ropes. A good agreement among the experimental test, the analytical model, and the numerical simulations can be observed. The differences in maximum elongation, mean extension of the dissipating devices, and energy dissipation allocation are all within a 10% margin. In the analytical model, a perfectly centred impact represents a symmetric condition, i.e., both Δ_X and Δ_Y are equal to zero. The symmetry in the X direction is largely confirmed by the experimental and numerical results. However, the results for Δ_Y indicate that the dissipating devices connected to the lower longitudinal wire ropes tend to elongate more than those connected to the upper ones. This is attributed to two main effects. Firstly, in the experimental test, an inclination between the net and the impact direction of approximately $\alpha \approx 30^\circ$ was observed, introducing a geometric asymmetry. Secondly, due to the broader contact area with the external post heads, the upper wire ropes are expected to experience an additional loss of force during sliding. These effects are not addressed in the current version of the analytical model, but their inclusion will be considered in future developments.

Table 3 illustrates the effect of uncertainties in the corrective parameters λ , η and γ on the key outputs of the model. For a generic input parameter X , a normalized sensitivity index S is calculated with respect to each output Y as follows:

$$S_X(Y) = \frac{Y(X + \sigma) - Y(X - \sigma)}{2\sigma} \frac{\mu_X}{Y(\mu)} \quad (17)$$

The sensitivity index obtained from Eq. (17) is dimensionless, but it can be interpreted as the percentage change in the output resulting from a 1% change in the input. The variation in the outputs is of the same order of magnitude as the variation in the input corrective coefficients. Notably, variations in λ have the largest impact on E_b and E_n , while variations in η significantly affect only E_n , as η is specific to the net. In the absence of dissipating devices on upslope ropes (as in RXI-100), γ does not affect any outputs other than $T_{max,s}$.

Fig. 19 shows the $F-w$ trend of the system as obtained from the analytical model. As expected, due to the absence of dissipating devices along the transversal ropes, the energy dissipation in the transversal substructures is negligible, accounting for approximately 0.5% of the

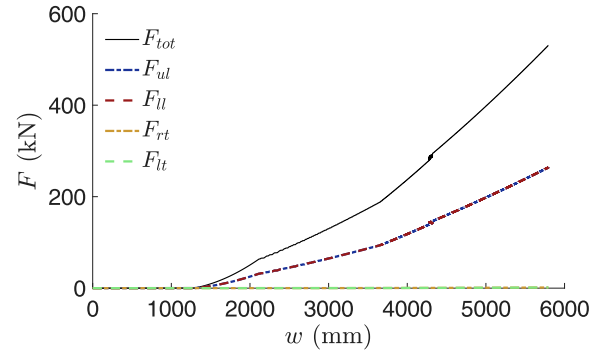


Fig. 19. Centred impact force–displacement behaviour using the analytical model.

total energy consumed. The symmetry of the problem in both the X and Y directions is confirmed by the results in terms of maximum forces in the panel wire ropes (Fig. 20(a)) and equivalent dissipating devices elongations (Fig. 20(b)). In the graphs, the initial phase represents the loading condition. This phase, up to approximately 1000 mm, also includes the initial deflection that the intercepting structure undergoes during the actual impact. Once the system is loaded, the tension force in the longitudinal wire ropes increases rapidly until it reaches the dissipating device activation threshold. At that point, occurring in the model at a displacement of around 2000 mm, devices are activated, dissipating energy, stabilizing the forces in the panel wire ropes, and providing flexibility to the system. In the absence of dissipating devices, the system would behave significantly more rigidly. As a result, the tension force in the longitudinal wire ropes would quickly reach their failure threshold, leading to system failure with a lower amount of energy dissipated.

Table 4 presents the results of the simulations for impact positions from 2 to 5, comparing both the analytical and numerical models, while the symmetric Mean Absolute Percentage Error (sMAPE), calculated as

$$sMAPE = \frac{|O_a - O_n|}{0.5(|O_a| + |O_n|)} \quad (18)$$

is shown in Table 5 for all the impacting positions analysed in this study. In Eq. (18), O_a and O_n represent the generic outputs provided respectively by the analytical and numerical models. The transversal eccentricity e_Y has a notable impact on the mechanical behaviour of rockfall barriers. As e_Y increases, the shortest load paths within the intercepting structure become progressively stiffer, leading to a reduction in the system's overall flexibility. When the impact occurs further from the centre in the transversal direction, small discrepancies emerge between the analytical and numerical models. These differences are mainly due to the greater influence of the assumptions made in the model formulation (see Section 2). Nevertheless, errors remains within a 10% margin for both energy absorption capacity and displacement at failure. Similarly, the longitudinal eccentricity e_X affects the system behaviour, especially when the system is impacted close to a steel post. Indeed, both the analytical and numerical models indicate that the system is able withstand the impact for load case 4 and fails to absorb the nominal impact energy for load case 5. Compared to the

Table 3
One-at-a-time sensitivity analysis for corrective parameters λ , η and γ .

Parameter	Case	w_{max}		E_b		E_n		$T_{max,l}$		$T_{max,s}$	
		(mm)	S (-)	(kJ)	S (-)	(kJ)	S (-)	(kN)	S (-)	(kN)	S (-)
λ (1.17 ± 0.02)	$\mu - \sigma$	5828	0.33	795.1	1.15	226.5	0.72	235.3	0.27	115.0	0.62
	$\mu + \sigma$	5762		764.7		221.0		233.1		112.6	
η (1.18 ± 0.07)	$\mu - \sigma$	5824	0.09	792.9	0.30	213.1	0.77	235.2	0.07	114.9	0.16
	$\mu + \sigma$	5763		765.6		233.5		233.2		112.7	
γ (1.19 ± 0.08)	$\mu - \sigma$	5795	0.00	779.9	0.00	223.7	0.00	234.2	0.00	106.2	1.00
	$\mu + \sigma$	5795		779.9		223.7		234.2		121.5	

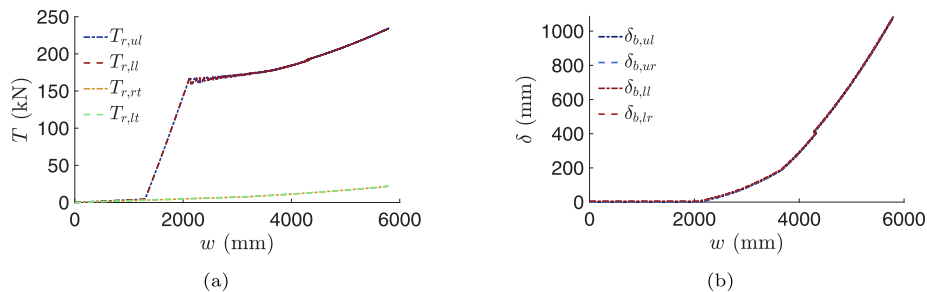


Fig. 20. Panel wire ropes maximum tension (a) and consequent dissipating device elongations (b)

Table 4
Analytical model validation for eccentric impacts.

Impact position	Output	Running time (h)	E_{tot} (kJ)	w_{max} (mm)	$\bar{\delta}$ (mm)	E_b (kJ)	E_n (kJ)	Δ_x (-)	Δ_y (-)
2	Num	4.37	1173.6	5531	953.9	672.4	252.3	0.00	0.05
	Anal	0.07	1099.5	5611	1006.4	726.1	207.4	0.00	0.26
3	Num	4.43	907.9	5032	723.5	492.9	188.0	0.00	0.05
	Anal	0.08	993.6	5153	756.1	612.8	176.1	0.00	0.50
4	Num	4.74	1171.4	5462	883.2	617.7	222.3	0.15	0.08
	Anal	0.08	1175.4	5597	1052.0	763.8	233.7	0.25	0
5	Num	4.63	836.8	4370	594.3	396.4	173.8	0.06	0.15
	Anal	0.08	713.1	4710	628.9	422.2	143.4	0.06	0.00

Table 5
Symmetric Mean Absolute Percentage Error (sMAPE) computed between the outputs of the numerical and analytical models for each impact position.

Impact position	sMAPE (%)				
	E_{tot}	w_{max}	$\bar{\delta}$	E_b	E_n
1	0.59	3.70	9.67	11.62	7.86
2	6.52	1.43	2.70	7.68	19.50
3	9.01	2.38	4.41	21.69	6.54
4	0.34	2.44	17.46	21.15	5.00
5	15.96	7.49	5.66	19.16	6.30

centred impact scenario (Table 2), the response is stiffer in both cases. For impact position 4, the same amount of energy is absorbed with a lower peak elongation. However, in the centred impact case, the system shows a significantly greater reserve of energy dissipation capacity. For impact position 5, flexibility is further limited by the complex combined response of longitudinal and transversal ropes, which also introduces greater uncertainty in the system response. In this particular case, the agreement between analytical and numerical predictions remains within a 15% margin. The observed failures are mainly caused by localized load concentrations within the intercepting structure, identified in the simulations as the system’s most critical component.

6. Conclusion

In this study, a novel analytical framework was proposed to evaluate the performance of rockfall barriers under generic impact conditions. Unlike existing approaches, which are often limited to specific impact positions or barrier technologies, the presented methodology adopts a general and adaptable perspective. By idealizing each component of the barrier as a mechanical subsystem and assembling them according to their real-world configuration, the model captures the complex interactions and energy dissipation mechanisms inherent to the system. For each subsystem, the resisting and energy-dissipating mechanisms were identified, along with the key variables that characterize these mechanisms, while the assembly process consisted of defining the links between the subsystems according to their connections and the load transfer path.

The proposed model was tailored, calibrated and validated in reference to a specific barrier, namely the RXI-100 by Geobru gg AG, for which results from a full-scale impact test at a specific position are available. As only one full-scale impact test is available, a numerical model of a three-module barrier was developed to validate the analytical model for impact scenarios differing from the centred configuration specified in the Swiss guidelines. Model validation was carried out for five different impact positions: a centred one and two eccentric impact

conditions along both the Y and X directions. For these cases, only the results from the numerical model are available. The presence of dissipating devices plays a crucial role in limiting forces within the wire ropes and the intercepting structure, which, based on the RXI-100 case study, emerges as the most critical component for system failure.

Overall, this multi-scale analytical model proves to be a reliable and efficient tool for evaluating a wide range of impact scenarios offering a valuable tool for design, optimization, and comparative analysis across different technologies. Despite its quasi-static nature, the key mechanical responses observed in real dynamic impact scenarios are effectively reproduced, as discrepancies in key parameters, such as elongation, energy dissipation, and force distribution, stand respectively within a 10% and a 15% margin for centred and eccentric impact conditions. Despite requiring calibration and validation, the limited number of needed full-scale or numerical tests significantly reduces experimental and computational demands, making the approach both practical and scalable for different barrier technologies. Once validated, the analytical model can be used to explore the full range of possible impact conditions and is easily adaptable to different barrier technologies, making it a powerful and cost-effective tool for comprehensive performance assessment. The potential energy dissipation for a given impact scenario can be estimated with a significant reduction in computational time (up to 98%) if compared with numerical simulations. This allows multiple analyses to be conducted within a reasonable timeframe, enabling efficient evaluations of performance.

For existing barriers, where one or more dissipating devices may have been partially or fully activated by previous impacts, the residual performance can be significantly reduced. In general, the load demand ratio, defined as the ratio between the load bore by the generic component and its maximum loading capacity, can be extracted at each computational step, allowing to identify the critical components for the generic impact condition analysed with the model. In real-world applications for post-impact evaluations, relevant information such as the impactor's shape and location is often retrievable through post-event inspections (e.g., visible net deformations or brake engagement levels). While direct measurement of the impact velocity is generally more challenging, it can be indirectly estimated by calibrating the model to reproduce the observed system response (e.g. net residual deformation, dissipating devices stroke). This modelling approach enables post-impact back-analysis, allowing for the reconstruction of likely impact conditions and, more importantly, for assessing the extent of structural damage. As such, the model may also support lifecycle assessment by informing decisions on maintenance needs and residual performance evaluation following an event.

Future developments may focus on validating the model through more experimental data and extending its capabilities to account for dynamic and force redistribution effects due to the rotation of the impactor and material non-linearities. Perspectives also include extending the analytical model to aged systems, where the initial load transmission by the intercepting structure may be significantly altered due to corrosion processes (Xu et al., 2024) or previous impact events. These changes can influence the mechanical response of the barrier, especially in systems where dissipating devices have already been partially or fully activated. Incorporating such considerations into the model holds strong potential for enhancing residual risk assessments (Marchelli et al., 2024), ultimately supporting public administrations in making more effective decisions regarding resource allocation and protective strategies against rockfall hazards.

Notation

e_x	Impact eccentricity on x-axis (m)
e_y	Impact eccentricity on y-axis (m)
f	Fibre number
i	Impacted module
j	Iteration number for each step
k	Steel net fibres secant stiffness (N/m)
l	Lateral modules
m	Number of fibres in transversal substructures
m_i	Impactor mass (kg)
$m_{i,p}$	Impactor participating mass (kg)
n	Number of fibres in longitudinal substructures
p	Step number in the analytical calculation
q	Generic force applied on panel wire ropes (N)
r	Total number of fibres
s	Panel steel wire rope line coordinate (m)
t	External modules
u_l	Upper longitudinal substructure
v	Panel steel wire ropes deflection (m)
w	Impactor displacement (m)
A	Wire ropes cross-sectional area (mq)
B	Dissipating devices load (N)
E_b	Energy dissipated by dissipating devices (J)
E_e	Energy stored due to elasticity (J)
E_{eq}	Wire ropes equivalent stiffness (N/m)
E_{fd}	Energy dissipated through friction (J)
E_i	Incident impact energy (J)
E_{int}	Dissipated internal energy (J)
E_{ks}	Kinetic energy of the protective structure (J)
E_N	Nominal energy of the barrier (J)
E_n	Energy dissipated by the intercepting structure (J)
O_a	Generic output provided by the analytical model
O_n	Generic output provided by the numerical model
E_{pd}	Energy dissipated by plastic deformation (J)
E_{tot}	Total consumed energy (J)
E_{vd}	Energy dissipated through visco-elastic processes (J)
F	Total force in Z direction (N)
H	Horizontal force in panel wire ropes (N)
K_s	Subsystem stiffness (N/m)
L	Steel net fibres length (m)
M_B	Rockfall barrier mass (kg)
$M_{B,p}$	Rockfall barrier participating mass (kg)
N	Axial force in steel net fibres (N)
Q	Force transmitted by steel net fibres to panel wire ropes (N)
R	Impactor radius (m)
R_{dx}	Reaction force at panel wire ropes right support (N)
S	Normalized sensitivity index (-)
T	Axial force in steel wire ropes (N)
$T.$	Axial force in steel wire ropes measured at the ground anchor (N)
T_μ	Friction force (N)
U_{max}	Ultimate capacity of the connection to the ground (N)
ll	Lower longitudinal substructure
lt	Left transversal substructure
rt	Right transversal substructure
α	Impacting angle (rad)
β	Spatial orientation of steel net fibres (rad)
Δl	Steel net fibres elongation (m)
Δ_X	Asymmetry parameter in the X direction
Δ_Y	Asymmetry parameter in the Y direction
Δ_{XY}	Combined asymmetry parameter
γ	Uneven load distribution factor for upslope ropes (-)

δ	Dissipating devices elongation (m)
η	Amplification factor for the energy dissipated by the net (-)
λ	Amplification factor for the total energy dissipation (-)
μ	Friction coefficient (-)
θ	Supporting post to wire rope contact angle (rad)
ω, ω'	Spatial orientation of steel net fibres (rad)
1, 2, 3, 4	Supporting steel posts

CRedit authorship contribution statement

Francesco Pimpinella: Writing – review & editing, Writing – original draft, Software, Methodology, Formal analysis, Conceptualization. **Maddalena Marchelli:** Writing – review & editing, Writing – original draft, Supervision, Methodology, Conceptualization. **Valerio De Biagi:** Writing – review & editing, Supervision, Methodology, Conceptualization.

Funding

This publication was produced while (F.P.) attending the PhD programme in Civil and Environmental Engineering at Politecnico di Torino, Cycle 38-th, with the support of a scholarship co-financed by the Ministerial Decree no. 352 of 9th April 2022, based on the NRRP - funded by the European Union - NextGenerationEU - Mission 4 “Education and Research”, Component 2 “From Research to Business”, Investment 3.3, and by GeobruGG AG. This work was also supported by (M.M) Marie Curie Postdoctoral Fellowship 2022 (Call Horizon-MSCA-2022-PF-01, grant GA101103401 - RIDETHERISK project) and (V.D.B) by the MUR – M4C2 1.5 of PNRR funded by the European Union - NextGenerationEU (project NODES grant agreement no. ECS00000036).

Declaration of competing interest

The authors declare that they have no known competing financial interests or personal relationships that could have appeared to influence the work reported in this paper.

Acknowledgements

We would like to thank GeobruGG AG and their members Dr Aron Vogel and Dr Roberto Jesùs Luis Fonseca for their cooperation in developing this work. The authors also thank the reviewers for their insightful observations and suggestions.

Data availability

Data will be made available on request.

References

- Blau, P.J., 2008. *Friction Science and Technology: From Concepts To Applications*. CRC Press.
- Bourrier, F., Lambert, S., Baroth, J., 2015. A reliability-based approach for the design of rockfall protection fences. *Rock Mech. Rock Eng.* 48 (1), 247–259. <http://dx.doi.org/10.1007/s00603-013-0540-2>.
- Cantarelli, G., Giani, G., 2006. *Analisi dei metodi di verifica dell'efficienza di reti di protezione contro la caduta di massi (in Italian)*. Assoc. Geotec. Ital. Luglio Settembre 2006, 23–31.
- Castanon-Jano, L., Blanco-Fernandez, E., Castro-Fresno, D., 2019. Design of a new energy dissipating device and verification for use in rockfall protection barriers. *Eng. Struct.* 199, 109633. <http://dx.doi.org/10.1016/j.engstruct.2019.109633>.
- Castanon-Jano, L., Blanco-Fernandez, E., Castro-Fresno, D., Ballester-Muñoz, F., 2017. Energy dissipating devices in falling rock protection barriers. *Rock Mech. Rock Eng.* 50, 603–619. <http://dx.doi.org/10.1007/s00603-016-1130-x>.
- Castro-Fresno, D., Del Coz Díaz, J., Nieto, P.G., Contreras, J.N., 2009. Comparative analysis of mechanical tensile tests and the explicit simulation of a brake energy dissipater by fem. *Int. J. Nonlinear Sci. Numer. Simul.* 10, 1059–1085. <http://dx.doi.org/10.1515/IJNSNS.2009.10.8.1059>.
- Caviezal, A., Munch, J., Bartelt, P., Lanter, A., 2022. Rockfall Barrier Service Loads for Rock Impacts with Spin. Vol. 125, WSL Berichte, <http://dx.doi.org/10.55419/wsl:32009>.
- Cazzani, A., Mongiovi, L., Frenez, T., 2002. Dynamic finite element analysis of interceptive devices for falling rocks. *Int. J. Rock Mech. Min. Sci.* 39, 303–321.
- Chen, Y., Qin, W., Wang, Q., Tan, H., 2021. Influence of corrosion pit on the tensile mechanical properties of a multi-layered wire rope strand. *Constr. Build. Mater.* 302, 124387. <http://dx.doi.org/10.1016/j.conbuildmat.2021.124387>.
- Coulibaly, J., Chanut, M.A., Lambert, S., Nicot, F., 2017. Nonlinear discrete mechanical model of steel rings. *Am. Soc. Civ. Eng.* 143 (9), [http://dx.doi.org/10.1061/\(ASCE\)EM.1943-7889.0001303](http://dx.doi.org/10.1061/(ASCE)EM.1943-7889.0001303).
- Coulibaly, J., Chanut, M.A., Lambert, S., Nicot, F., 2018. Sliding cable modeling: an attempt at a unified formulation. *Int. J. Solids Struct.* 130–131, 1–10. <http://dx.doi.org/10.1016/j.ijsolstr.2017.10.025>.
- Coulibaly, J., Chanut, M.A., Lambert, S., Nicot, F., 2019. Toward a generic computational approach for flexible rockfall barrier modeling. *Rock Mech. Rock Eng.* 52, 4475–4496. <http://dx.doi.org/10.1007/s00603-019-01878-6>.
- De Menezes, E., Marczak, R., 2021. Comparative analysis of different approaches for computing axial, torsional and bending stiffnesses of cables and wire ropes. *Eng. Struct.* 241, 112487. <http://dx.doi.org/10.1016/j.engstruct.2021.112487>.
- Dhakal, J., Bhandary, N., Yatabe, R., Kinoshita, N., 2012. Numerical and analytical investigation towards performance enhancement of a newly developed rockfall protective cable-net structure. *Nat. Hazards Earth Syst. Sci.* 12, 1135–1149. <http://dx.doi.org/10.5194/nhess-12-1135-2012>.
- Douthe, C., Girardon, C., Boulaud, R., 2022. Enhanced damage modelling of steel wire ring nets subjected to repeated rockfall impacts. *Geosci.* 12 (2), 75. <http://dx.doi.org/10.3390/geosciences12020075>.
- EAD 340059-00-0106, 2018. *Falling Rock Protection Kits. EOTA - European Organisation for Technical Assessment*.
- Eicher, M., Fonseca, R.L., Lanter, H., 2023. Considering fragmentation and variability of rockfall and the third dimension in rockfall barrier design. In: *Rocscience International Conference. RIC 2023*, Atlantis Press, pp. 799–805.
- EN 1997-1:2004, 2004. *Eurocode 7 - Geotechnical design. Part 1: General rules*.
- Escallón, J., Wendeler, C., Chatzi, E., Bartelt, P., 2014. Parameter identification of rockfall protection barrier components through an inverse formulation. *Eng. Struct.* 77, 1–16. <http://dx.doi.org/10.1016/j.engstruct.2014.07.019>.
- Feyrer, K., 2007. *Wire Ropes, Tension, Endurance, Reliability*. Springer.
- Forni, D., Chiaia, B., Cadoni, E., 2016. Strain rate behaviour in tension of s355 steel: Base for progressive collapse analysis. *Eng. Struct.* 119, 164–173. <http://dx.doi.org/10.1016/j.engstruct.2016.04.013>.
- Fulde, M., Müller, M., 2013. Development of a modular brake element for the use in modern rockfall catchment fences. In: *Proceedings of the 64th Highway Geology Symposium*. pp. 297–314.
- Gentilini, C., Gottardi, G., Govoni, L., Mentani, A., Ubertini, F., 2013. Design of falling rock protection barriers using numerical models. *Eng. Struct.* 50, 96–106. <http://dx.doi.org/10.1016/j.engstruct.2012.07.008>.
- Gentilini, C., Govoni, L., De Miranda, S., Gottardi, G., Ubertini, F., 2012. Three-dimensional numerical modelling of falling rock protection barriers. *Comput. Geotech.* 44, 58–72. <http://dx.doi.org/10.1016/j.compgeo.2012.03.011>.
- Gerber, W., 2001. *Guideline for the Approval of Rockfall Protection Kits. Swiss Agency for the Environment, Forests and Landscape (SAEFL) and the Swiss Federal Research Institute*.
- Guo, L., Yu, Z., He, S., Jin, Y., Jian, J., 2024. Enhanced damage modelling of steel wire ring nets subjected to repeated rockfall impacts. *Comput. Geotech.* 176, 106760. <http://dx.doi.org/10.1016/j.compgeo.2024.106760>.
- Guo, L., Yu, Z., Jin, Y., Liao, L., Luo, L., 2022. An analytical method for evaluating the deflection and energy absorption capacity of rockfall ring nets considering multifactor influence. *Adv. Steel Constr.* 18, 630–647. <http://dx.doi.org/10.18057/IJASC.2022.18.3.1>.
- Guo, L., Yu, Z., Luo, L., Qi, X., Zhao, S., 2020. An analytical method of puncture mechanical behaviour of ring nets based on the load path equivalence (in Chinese). *Gong Cheng Li Xue Eng. Mech.* 37 (5), 129–139. <http://dx.doi.org/10.6052/j.issn.1000-4750.2019.07.0345>.
- Hambleton, J., Buzzi, O., Giacomini, A., Spadari, M., Sloan, S., 2012. Perforation of flexible rockfall barriers by normal block impact. *Rock Mech. Rock Eng.* 46, 515–526. <http://dx.doi.org/10.1007/s00603-012-0343-x>.
- Han, Y., Yuan, C., Li, S., Feng, X., Dong, F., Li, J., 2025. Experimental and theoretical analysis of the mechanical characteristics of optimized chain-link structural meshes improved with steel strands. *Struct.* 76, 108929. <http://dx.doi.org/10.1016/j.istruc.2025.108929>.
- ISO 12076, 2002. *ISO 12076:2002 steel wire ropes — Determination of the actual modulus of elasticity*.
- ISO 17745, 2016. *ISO 17745:2016 Steel Wire Ring Net Panels – Definitions and Specifications. International Organization for Standardization*.
- Jin, Y., Yu, Z., Luo, L., Guo, L., Zhang, L., 2021. A membrane equivalent method to reproduce the macroscopic mechanical responses of steel wire-ring nets under rockfall impact. *Thin-Walled Struct.* 167, 108227. <http://dx.doi.org/10.1016/j.tws.2021.108227>.
- Karampinos, E., Hadjigeorgiou, J., 2021. Quantifying the impact of bolting patterns on the performance of welded wire mesh. *Geotech. Geol. Eng.* 39, 359–376.

- Koo, R., Kwan, J., Lam, C., Ng, C., Yiu, J., Choi, C., Ng, A., Ho, K., Pun, W., 2016. Dynamic response of flexible rockfall barriers under different loading geometries. *Landslides* 14, 905–916. <http://dx.doi.org/10.1007/s10346-016-0772-9>.
- Lambert, S., Toe, D., Mentani, A., Bourrier, F., 2020. A meta-model-based procedure for quantifying the on-site efficiency of rockfall barriers. *Rock Mech. Rock Eng.* 54, 487–500. <http://dx.doi.org/10.1007/s00603-020-02298-7>.
- Lu, G., Yu, T., 2003. *Energy Absorption of Structures and Materials*. Elsevier.
- Maheshwari, S., Bhowmik, R., Samanta, M., 2023. Rockfall hazard: A comprehensive review of current mitigation practices. In: *Landslides: Detection, Prediction and Monitoring: Technological Developments*. Vol. 2023, pp. 175–209. http://dx.doi.org/10.1007/978-3-031-23859-8_9.
- Marchelli, M., De Biagi, V., Chiaia, B., 2024. A fully probabilistic framework to compute the residual rockfall risk in presence of mitigation measures. *Landslides* <http://dx.doi.org/10.1007/s10346-024-02377-8>.
- Marchelli, M., Pol, A., Peila, D., Gabrieli, F., 2023. Towards a hybrid design approach of anchored drapery systems. *Geosci.* 13 (147).
- Mentani, A., 2015. Modelling the dynamic response of rockfall protection barriers. URL: <https://api.semanticscholar.org/CorpusID:106590441>.
- Mentani, A., Giacomini, A., Buzzi, O., Govoni, L., Gottardi, G., S. F., 2015. Numerical modelling of a low-energy rockfall barrier: New insight into the bullet effect. *Rock Mech. Rock Eng.* 49, 1247–1262.
- Mentani, A., Govoni, L., Giacomini, A., Gottardi, G., Buzzi, O., 2018. An equivalent continuum approach to efficiently model the response of steel wire meshes to rockfall impacts. *Rock Mech. Rock Eng.* 51 (3), 2826–2838. <http://dx.doi.org/10.1007/s00603-018-1490-5>.
- Mentani, A., Govoni, L., Gottardi, G., Toe, D. and Lambert, S., Bourrier, F., 2017. Sviluppo di un metamodello del comportamento di opere di mitigazione del rischio di caduta massi. In: *Atti Dell'Incontro Annuale Dei Ricercatori Di Geotecnica – IARG 2017*. pp. 1–6.
- Nelder, J., Mead, R., 1965. A simplex method for function minimization. *Comput. J.* 7 (4), 308–313. <http://dx.doi.org/10.1093/comjnl/7.4.308>.
- Osairan, A., Chanut, M., Bost, M., Pruvost, C., Verdet, M., Dugelas, L., 2025. Highlighting the dynamic effect on dissipator by friction installed in flexible barriers. *Rock Mech. Rock Eng.* <http://dx.doi.org/10.1007/s00603-025-04646-x>.
- Peila, D., Pelizza, S., Sassudelli, F., 1998. Evaluation of behaviour of rockfall restraining nets by full scale tests. *Rock Mech. Rock Eng.* 31, 1–24.
- Peila, D., Ronco, C., 2009. Design of rockfall net fences and the new etag 027 European guideline. *Nat. Hazards Earth Syst. Sci.* 9, 1291–1298.
- Pimpinella, F., Marchelli, M., De Biagi, V., 2024a. A weight-based efficiency measure for energy dissipating devices for flexible rockfall barriers. *Int. J. Prot. Struct.* <http://dx.doi.org/10.1177/20414196241299126>.
- Pimpinella, F., Marchelli, M., De Biagi, V., 2025. Effects of eccentric impacts and corrosion on the structural behaviour of retaining wire ring nets. In: *Proceedings of the 7th International Conference on Protective Structures*.
- Pimpinella, F., Marchelli, M., Lanter, A., De Biagi, V., 2024b. Numerical back-analysis of impacted rockfall barriers steel posts: discussion on the effectiveness of the system. In: *Proceedings of the XIVth International Symposium on Landslides*.
- Pol, A., Gabrieli, F., Brezzi, L., 2021a. Discrete element analysis of the punching behaviour of a secured drapery system: from laboratory characterization to idealized in situ conditions. *Acta Geotech.* 16, 2553–2573.
- Pol, A., Gabrieli, F., Brezzi, L., 2021b. Discrete element analysis of the punching behaviour of a secured drapery system: from laboratory characterization to idealized in situ conditions. *Acta Geotech.* 16 (8), 2553–2573. <http://dx.doi.org/10.1007/s11440-020-01119-z>.
- Qi, X., Pei, X., Han, R., Yang, Y., Meng, Q., Yu, Z., 2018a. Analysis of the effects of a rotating rock on rockfall protection barriers. *Geotech. Geol. Eng.* 36, 3255–3267. <http://dx.doi.org/10.1007/s10706-018-0535-6>.
- Qi, X., Yu, Z., Zhao, L., Xu, H., 2018b. A new numerical modelling approach for flexible rockfall protection barriers based on failure modes. *Adv. Steel Constr.* 14, 479–495. <http://dx.doi.org/10.18057/IJASC.2018.14.3.10>.
- Qi, X., Yu, Z., Zhao, L., Xu, H., Meng, Q., 2018c. Dynamic mechanical property study of break rings in flexible protective system (in Chinese). *Gongcheng Lixue Eng. Mech.* 35, 188–196. <http://dx.doi.org/10.6052/j.issn.1000-4750.2017.06.0438>.
- Ribeiro, J., Santiago, A., Rigueiro, C., 2016. Damage model calibration and application for s355 steel. *Procedia Struct. Integr.* 2, 656–663. <http://dx.doi.org/10.1016/j.prostr.2016.06.085>.
- Spadari, M., Giacomini, A., Buzzi, O., Hambleton, J., 2011. Prediction of the bullet effect for rockfall barriers: a scaling approach. *Rock Mech. Rock Eng.* 45, 131–144. <http://dx.doi.org/10.1007/s00603-011-0203-0>.
- Toe, D., Mentani, A., Govoni, L., Bourrier, F., Gottardi, G., Lambert, S., 2018. Introducing meta-models for a more efficient hazard mitigation strategy with rockfall protection barriers. *Rock Mech. Rock Eng.* 51, 1097–1109. <http://dx.doi.org/10.1007/s00603-017-1394-9>.
- Trad, A., Limam, A., Bertrand, D., Robit, P., 2013. Multi-scale analysis of an innovative flexible rockfall barrier. *Rockfall Eng.* 303–342. <http://dx.doi.org/10.1002/9781118601532.ch9>.
- UNI 11437, 2012. *Opere Di Difesa Dalla Caduta Massi - Prove Su Reti Per Rivestimento Di Versanti. UNI (Ente Nazionale Italiano di Unificazione)*.
- Van Tran, P., Maegawa, K., Fukada, S., 2012. Experiments and dynamic finite element analysis of a wire-rope rockfall protective fence. *Rock Mech. Rock Eng.* 46, 1183–1198. <http://dx.doi.org/10.1007/s00603-012-0340-0>.
- Van Tran, P., Maegawa, K., Fukada, S., 2013. Prototype of a wire-rope rockfall protective fence developed with three-dimensional numerical modeling. *Comput. Geotech.* 54, 84–93. <http://dx.doi.org/10.1016/j.compgeo.2013.06.008>.
- Volkwein, A., Roth, A., Gerber, W., Vogel, A., 2009. Flexible rockfall barriers subjected to extreme loads. *Struct. Eng. Int.* 19, 327–332. <http://dx.doi.org/10.2749/101686609788957900>.
- Volkwein, A., Schellenberg, K., Labiouse, V., Agliardi, F., Berger, F., Bourrier, F., Dorren, L.K., Gerber, W., Jaboyedoff, M., 2011. Rockfall characterisation and structural protection—a review. *Nat. Hazards Earth Syst. Sci.* 11, 2617–2651. <http://dx.doi.org/10.5194/nhess-11-2617-2011>.
- Wang, X., Meng, X., Wang, J., Sun, Y., Gao, K., 2015. Mathematical modeling and geometric analysis for wire rope strands. *Appl. Math. Model.* 39, 1019–1032. <http://dx.doi.org/10.1016/j.apm.2014.07.015>.
- Xu, H., Gentilini, C., Yu, Z., Qi, X., Zhao, S., 2018a. An energy allocation based design approach for flexible rockfall protection barriers. *Eng. Struct.* 173, 831–852. <http://dx.doi.org/10.1016/j.engstruct.2018.07.018>.
- Xu, H., Gentilini, C., Yu, Z., Qi, X., Zhao, S., 2018b. An energy allocation based design approach for flexible rockfall protection barriers. *Eng. Struct.* 173, 831–852. <http://dx.doi.org/10.1016/j.engstruct.2018.07.018>.
- Xu, H., Yang, C., Zhao, L., Yupeng, L., Zhixiang, Y., 2024. Experimental study on bearing capacity reduction of the steel wire-rings in flexible barriers due to corrosion. *Constr. Build. Mater.* 439, 137341. <http://dx.doi.org/10.1016/j.conbuildmat.2024.137341>.
- Yang, J., Duan, S., Li, Q., Chengqing, L., 2019. A review of flexible protection in rockfall protection. *Comput. Geotech.* 99 (1), 89–99. <http://dx.doi.org/10.1007/s11069-019-03709-x>.
- Yu, Z., Luo, L., Liu, C., Guo, L., Qi, X., Zhao, L., 2021. Dynamic response of flexible rockfall barriers with different block shapes. *Landslides* 18, 2621–2637. <http://dx.doi.org/10.1007/s10346-021-01658-w>.
- Yu, Z., Qiao, Y., Zhao, L., Xu, H., Zhao, S., Liu, Y., 2018. A simple analytical method for evaluation of flexible rockfall barrier part 1: working mechanism and analytical solution. *Adv. Steel Constr.* 14, 115–141. <http://dx.doi.org/10.18057/IJASC.2018.14.2.1>.
- Zhang, L., Yu, Z., Luo, L., Liao, L., Jin, Y., Xu, H., 2023. An evaluation method for quantifying the residual performance of flexible rockfall barriers after impact. *Int. J. Impact Eng.* 181, 104766. <http://dx.doi.org/10.1016/j.ijimpeng.2023.104766>.
- Zhao, L., Hao, C., Yu, Z., Zhao, S., 2022a. Numerical simulation of dynamic responses of semi-rigid rockfall protection barriers subjected to impact loading at different positions. *Bull. Eng. Geol. Environ.* 81 (9), 367. <http://dx.doi.org/10.1007/s10064-022-02870-1>.
- Zhao, L., Yu, Z.X., Liu, Y.P., He, J.W., Chan, S.L., Zhao, S.C., 2020. Numerical simulation of responses of flexible rockfall barriers under impact loading at different positions. *J. Constr. Steel Res.* 167, 105953. <http://dx.doi.org/10.1016/j.jcsr.2020.105953>.
- Zhao, L., Zhang, L., Yu, Z., Qi, Z., Xu, H., Zhang, Y., 2022b. A case study on the energy capacity of a flexible rockfall barrier in resisting landslide debris. *Forests* 13 (9), 1384. <http://dx.doi.org/10.3390/f13091384>, 2022.